ARTICLES
https://doi.org/10.1038/s41563-020-0783-8

nature materials

Check for updates

ILC1 drive intestinal epithelial and matrix remodelling

Geraldine M. Jowett[1,2,3,4], Michael D. A. Norman[1,19], Tracy T. L. Yu[1,19], Patricia Rosell Arévalo[2], Dominique Hoogland[5], Suzette T. Lust[1], Emily Read[2,3], Eva Hamrud[1,3,4], Nick J. Walters[6,7], Umar Niazi[8], Matthew Wai Heng Chung[2,3,4], Daniele Marciano[1], Omer S. Omer[9,10], Tomasz Zabinski[2], Davide Danovi[4], Graham M. Lord[11], Jöns Hilborn[12], Nicholas D. Evans[13], Cécile A. Dreiss[14], Laurent Bozec[15], Oommen P. Oommen[16], Christian D. Lorenz[17], Ricardo M. P. da Silva[1,18], Joana F. Neves[2,19] ✉ and Eileen Gentleman[1,19] ✉

Organoids can shed light on the dynamic interplay between complex tissues and rare cell types within a controlled microenvironment. Here, we develop gut organoid cocultures with type-1 innate lymphoid cells (ILC1) to dissect the impact of their accumulation in inflamed intestines. We demonstrate that murine and human ILC1 secrete transforming growth factor β1, driving expansion of CD44v6$^+$ epithelial crypts. ILC1 additionally express MMP9 and drive gene signatures indicative of extracellular matrix remodelling. We therefore encapsulated human epithelial–mesenchymal intestinal organoids in MMP-sensitive, synthetic hydrogels designed to form efficient networks at low polymer concentrations. Harnessing this defined system, we demonstrate that ILC1 drive matrix softening and stiffening, which we suggest occurs through balanced matrix degradation and deposition. Our platform enabled us to elucidate previously undescribed interactions between ILC1 and their microenvironment, which suggest that they may exacerbate fibrosis and tumour growth when enriched in inflamed patient tissues.

Intestinal epithelial cells (IEC)[1] interact with innate lymphoid cells (ILC)[2] to form a dynamic barrier between organisms and their environment. Together, they are capable of rapidly responding to danger and damage in an antigen-non-specific manner. For instance, type-3 ILC secrete interleukin-22 (IL-22, *Il22*) in response to extracellular pathogens, which promotes antimicrobial peptide secretion and proliferation of Lgr5$^+$ CD44$^+$ intestinal stem cells[3]. Conversely, type-1 ILC (ILC1) express interferon-γ (IFN-γ, *Ifng*) in response to intracellular pathogens, and are composed of circulating natural killer (NK) cells and tissue-resident helper-like ILC1, which are considered less cytotoxic than their NK-cell counterparts[4]. Notably, ILC1 accumulate in the inflamed intestines of patients with inflammatory bowel disease (IBD)[5]; however, the nature of their subset-specific interactions with the epithelium has remained elusive. Understanding the impact of ILC1 enrichment could inform alternative strategies for treating this complex disease, which is a pressing issue as only a third of patients respond to gold-standard tumour-necrosis factor (TNF)-α-blocking biologics[6].

Teasing apart the role of rare cell populations in multifactorial diseases is challenging, and redundant cytokine signalling pathways in vivo can obscure ILC-specific phenotypes. Thus, to explore the impact of ILC1 on IEC we developed a reductionist coculture system with murine small intestine organoids (SIO)[7]. We unexpectedly found that ILC1-derived transforming growth factor (TGF) β1 induces p38γ phosphorylation, driving proliferation of CD44v6$^+$ epithelial cells. Moreover, pathway analysis of coculture transcriptomes predicted ILC1-driven matrisome remodelling, so we developed highly defined polyethylene glycol (PEG)-based hydrogels to quantitatively characterize the impact of ILC1 on matrix remodelling in a human induced pluripotent stem cell (iPSC)-derived organoid model (HIO)[8]. We confirmed not only that ILC1 derived from patients with IBD express *TGFB1* to upregulate intestinal CD44v6, but also that they prompt physical changes in the hydrogel via both degradation and production of peri-organoid matrix. Our findings suggest an unexpected role for ILC1 in intestinal remodelling, which could exacerbate IBD-associated comorbidities when enriched in inflamed intestines.

[1]Centre for Craniofacial and Regenerative Biology, King's College London, London, UK. [2]Centre for Host Microbiome Interactions, King's College London, London, UK. [3]Wellcome Trust Cell Therapies and Regenerative Medicine PhD Programme, London, UK. [4]Centre for Stem Cells & Regenerative Medicine, King's College London, London, UK. [5]Department of Chemistry, King's College London, London, UK. [6]BioMediTech, Tampere University Tampere Finland, Helsinki, Finland. [7]Natural Resources Institute Finland, Helsinki, Finland. [8]Guy's and St Thomas' National Health Service Foundation Trust and King's College London National Institute for Health Research Biomedical Research Centre Translational Bioinformatics Platform, Guy's Hospital, London, UK. [9]School of Immunology and Microbial Sciences, King's College London, London, UK. [10]Department of Gastroenterology, Guy's and St Thomas' Hospitals NHS Trust, London, UK. [11]Faculty of Biology, Medicine and Health, University of Manchester, Manchester, UK. [12]Department of Chemistry, Ångström Laboratory, Uppsala University, Uppsala, Sweden. [13]Bone and Joint Research Group, Centre for Human Development, Stem Cells and Regeneration, Human Development and Health, Institute of Developmental Sciences, University of Southampton, Southampton, UK. [14]Institute of Pharmaceutical Science, King's College London, London, UK. [15]Faculty of Dentistry, University of Toronto, Toronto, Ontario, Canada. [16]Bioengineering and Nanomedicine Lab, Faculty of Medicine and Health Technology, Tampere University, Tampere, Finland. [17]Department of Physics, King's College London, London, UK. [18]i3S—Instituto de Investigação e Inovação em Saúde—and INEB—Instituto de Engenharia Biomédica, Universidade do Porto, Porto, Portugal. [19]These authors contributed equally: Michael D. A. Norman, Tracy T. L. Yu, Joana F. Neves, Eileen Gentleman. ✉e-mail: joana.pereira_das_neves@kcl.ac.uk; eileen.gentleman@kcl.ac.uk

Results

ILC1 drive CD44$^+$ crypt expansion. To study the impact of ILC1 accumulation on IEC, we established cocultures of murine SIO and small intestinal lamina propria-derived ILC1 (Fig. 1a–c and Supplementary Fig. 1). ILC1 maintained characteristic KLRG1$^-$, RORγt$^-$, NK1.1$^+$ expression after coculture (Supplementary Figs. 2 and 3a), and expressed *Ifng*, but not *Il22*, matching freshly isolated ILC1 (Fig. 1d). We tuned this system to contain low levels of IFN-γ secretion (Supplementary Fig. 3b,c), and cultured SIO either alone or with ILC1 for 4 days. We then purified IEC using fluorescence-activated cell sorting (FACS) for bulk Smart-seq2 Pico RNA sequencing (RNA-seq). ILC1 coculture significantly increased expression of epithelial *Cd44*, a common crypt stem cell marker that can act as a growth factor coreceptor or a transcription factor, or mediate cell-surface adhesion[9] (Fig. 1e, Supplementary Fig. 2 and Supplementary Dataset 1). ILC1 also promoted the growth of enlarged CD44$^+$ crypt buds (Fig. 1f–h). To explore whether IFN-γ drove this effect, we supplemented SIO-only cultures with recombinant IFN-γ, which did not increase epithelial proliferation or *Cd44* expression (Fig. 1i,j). Moreover, Ingenuity Pathway Analysis (IPA) of the Smart-Seq2 dataset did not predict IFN-γ activity as a dominant signature of ILC1 coculture (Fig. 1k), suggesting that ILC1 upregulate CD44 through an alternative mechanism.

ILC1 secrete TGF-β1. As predicted by the IPA upstream regulators, we detected increased levels of TGF-β1 in the ILC1 coculture supernatants (Fig. 2a). Stimulated ILC1 expressed *Tgfb1* before and after coculture (Fig. 2b), mimicking expression patterns of *Ifng* (Fig. 1d). Although epithelial cells can express *Tgfb1* in response to microbiome metabolites[10], IEC expression of *Tgfb1* was negligible both with and without ILC1 coculture (Fig. 2c). However, SIO in our system maintained expression of TGF-β receptor 1 (TGF-βR1) (Fig. 2d), and broadly upregulated this receptor across the entire epithelium in ILC1 cocultures (Supplementary Fig. 4), indicating that SIO retained the capacity to respond to exogenous TGF-β1.

We next investigated whether TGF-β1 accounted for CD44 upregulation. First, we established that the phenotype was not contact dependent (Supplementary Fig. 5). We then distinguished between common splice isoforms of CD44 using intron-specific primers[11] and found that ILC1 coculture specifically upregulated CD44 variant 6 (*Cd44v6*), which was inhibited by TGF-β1,2,3 neutralizing antibody and upregulated by recombinant TGF-β1 in SIO-only cultures (Fig. 2e). Importantly, TGF-β1,2,3 inhibition did not adversely impact ILC1 viability or phenotype (Supplementary Fig. 6). CD44v6 protein was ubiquitously distributed across the basolateral membrane of the SIO crypt in cocultures (Fig. 2f), and did not appear to concentrate in specific IEC subsets. TGF-β1-induced expression of CD44v6 has been described in fibrotic lung fibroblasts[12]; here, we describe such a connection in the intestinal epithelium.

CD44 engages in a positive feedback loop with Wnt/β-catenin. Indeed, it is a downstream target of β-catenin, and clusters with Lrp6 to potentiate Wnt signalling[13]. Moreover, IPA predicted significant increases in both p38/MAPK and Wnt/β-catenin signalling in SIO cocultured with ILC1 (Fig. 2g). We observed accumulation of epithelial β-catenin in ILC1 cocultures (Fig. 2h), and increased expression of β-catenin targets *Ascl2* and *Axin2* (Supplementary Fig. 7a). β-catenin accumulation colocalized with CD44v6$^+$ expression (Supplementary Fig. 7b), and was reversible by TGF-β1,2,3 neutralization (Fig. 2i). We first hypothesized that increased crypt size in ILC1 cocultures could be driven by CD44/β-catenin-induced modulation of IEC differentiation; however, despite a trending bias toward expression of stem cell crypt over mature enterocyte markers, differences in subset-specific genes were not statistically significant (Supplementary Fig. 8). Instead, IEC that upregulated CD44v6 and β-catenin also showed a dramatic increase in phosphorylated p38 signal (Fig. 2h), which was also upregulated by ILC1 coculture and downregulated through TGF-β1,2,3 neutralization (Fig. 2j). This kinase exists in multiple isoforms, with p38α/β regulating apoptosis and p38γ promoting proliferation. To investigate which isoform was active in our cocultures, we used the p38α/β inhibitor PD169316 (PD16) and p38γ inhibitor pirfenidone, a drug approved for the treatment of pulmonary fibrosis[14]. These soluble inhibitors impacted ILC1 phenotypes (Supplementary Fig. 9a), so we mimicked ILC1 coculture through addition of recombinant TGF-β1. SIO cultured with pirfenidone, but not PD16, significantly and specifically downregulated *Cd44v6* (Fig. 2k and Supplementary Fig. 9b) and *Axin2* (Fig. 2l), and reversed crypt budding, as did TGF-β1,2,3 neutralization (Fig. 2m). It is reported that p38γ phosphorylates the Ser-605 residue of β-catenin, thus stabilizing this mitogenic transcription factor, and driving inflammation-associated intestinal tumorigenesis[15]. This suggests that p38γ activity probably acts downstream of TGF-β1 and upstream of β-catenin and CD44v6 upregulation in our cocultures, which could promote IEC-subtype-non-specific proliferation and organoid growth through a positive CD44v6/β-catenin feedback loop.

ILC1 from patients with IBD upregulate intestinal CD44v6. Next, we isolated human intestinal lamina propria ILC1 (hILC1) from biopsies of patients with IBD (Supplementary Fig. 10), and established cocultures with human gut organoids (Supplementary Figs. 11 and 12). Epithelial-only biopsy-derived enteroids[16] closely mimic SIO, but, as these maintain epigenetic signatures of their donors[17], they offer no control over patients' genetic background or exposure to environmental stressors, diet or drugs. Conversely, differentiation[18] and maturation[19] of HIO provides greater control over genetics and environment, which are necessary for modelling multifactorial diseases. Following 7-day coculture with HIO, hILC1 maintained their phenotypic response to activation, upregulating *IFNG* but not *IL22* (Fig. 3a). In this system, hILC1 coculture increased basolateral CD44v6 expression in HIO IEC (Fig. 3b), which was recapitulated through addition of recombinant TGF-β1 (Supplementary Fig. 13). Strikingly, the increase in *CD44v6* expression was only statistically significant when hILC1 were derived from sites of active inflammation (Fig. 3c), which yielded more ILC1, recapitulating the previously reported[5] accumulation of this ILC subset (Fig. 3d, Supplementary Fig. 10). Intriguingly, hILC1 from inflamed tissues also proliferated more in coculture than those from uninflamed biopsies (Fig. 3e). This suggests that the inflamed IBD microenvironment left a proliferative imprint on hILC1, which was maintained ex vivo in a reductionist system with constant intestinal genetics, cytokine exposure, environmental stimuli and microbiome composition. However, hILC1 from both conditions expressed *TGFB1* before (Supplementary Fig. 14) and after coculture with HIO (Fig. 3f), and expression levels did not differ significantly between cultures from inflamed and uninflamed tissues. We therefore suggest that the differential upregulation of *CD44v6* in inflamed cocultures resulted from the increased number of hILC1 in this system, not from cell-intrinsic differences in *TGFB1* expression. Thus, hILC1 from patients with inflamed IBD provide a disease-relevant in vitro model of the impact of hILC1 accumulation on the gut, allowing us to appropriately explore murine coculture data in a translationally relevant system.

To confirm the clinical relevance of data obtained in this system, we performed immunohistochemistry on inflamed and uninflamed intestinal biopsies. We observed an increase in epithelial CD44v6 expression along the basolateral junctions of enlarged crypts in inflamed tissues. This underscored that cocultures of SIO + ILC1 and HIO + hILC1 (from patients with active inflammation) both predicted and recapitulated CD44v6 upregulation in inflamed IBD tissues. However, we also noticed CD44v6 expression beyond the epithelial compartment in the inflamed sections, both in CD45$^+$ lymphocytes and in basal lamina fibroblasts (Fig. 3g).

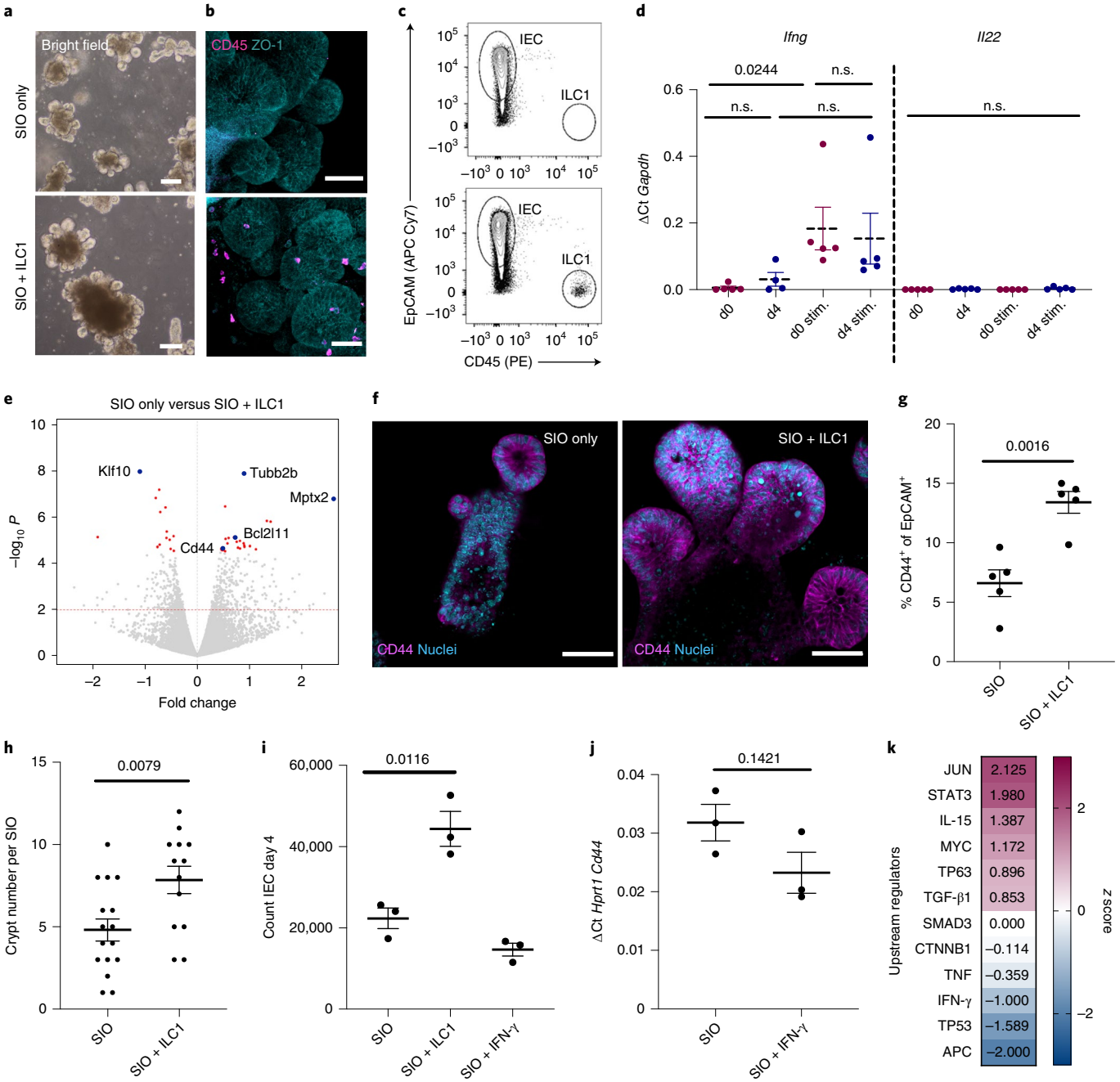

Fig. 1 | ILC1 impact intestinal organoid gene expression. a–c, Bright-field images (**a**), confocal microscopy images (**b**) and FACS plots (**c**) of SIO cultured alone (top) or with ILC1 (bottom) (representative of experiments with ILC1 from $N=3$ mice). **d**, Relative expression of *Ifng* and *Il22* in ILC1 normalized to housekeeping gene *Gapdh* before ($N=5$ mice, freshly isolated) and after (ILC1 from $N=4$ mice) coculture with SIO, each condition with or without 2-h stimulation with 10-ng-ml^{-1} phorbol myristate acetate (PMA) and 1-μM ionomycin (stim.). n.s., not significant. **e**, Volcano plot ($\log_{10}$ of the adjusted *p*-value p_{adj} versus fold change) of differentially expressed genes in the RNA-seq dataset, with significantly upregulated genes of interest highlighted with a blue circle (*P* values calculated using the Markov chain Monte Carlo simulation with multiple testing correction). **f**, Confocal microscopy images of SIO showing CD44$^+$ crypts with Lysozyme1$^+$ (Lyz1) Paneth cells (representative of $N=3$). **g**, Flow quantification of CD44 expression in IEC (ILC1 from $N=5$ mice). **h**, Quantification of crypt bud number per SIO (ILC1 derived from $N=3$ mice; each symbol represents one organoid). **i**, Number of EpCAM$^+$CD45$^-$ IEC in SIO after 4-day coculture alone, with ILC1 or with 0.01-ng-ml^{-1} IFN-γ (ILC1 from $N=3$ mice). **j**, Quantitative PCR with reverse transcription (RT-qPCR) of IEC *Cd44* expression with or without 0.01-ng-ml^{-1} IFN-γ ($N=3$ independent experiments). **k**. IPA of selected upstream regulators predicted to be driving expression signatures in ILC1 cocultures; *z* score magenta predicts high activity, blue predicts low activity. Horizontal lines beneath *p*-values delineate which two conditions are being compared within a statistical test. **a**,**b**,**f**, Scale bars, 50 μm. **d**,**g**–**j**, Unpaired two-tailed *t*-test *P* values between conditions; error bars, s.e.m.

Since inflamed tissues are infiltrated by many different immune cells, we could not determine whether the apparent mesenchymal upregulation was related to hILC1 accumulation, and therefore returned to the HIO model. HIO codevelop with organized layers of mesenchymal fibroblasts, closely mimicking the extracellular matrix (ECM) environment of the native intestine (Fig. 3h). We found that

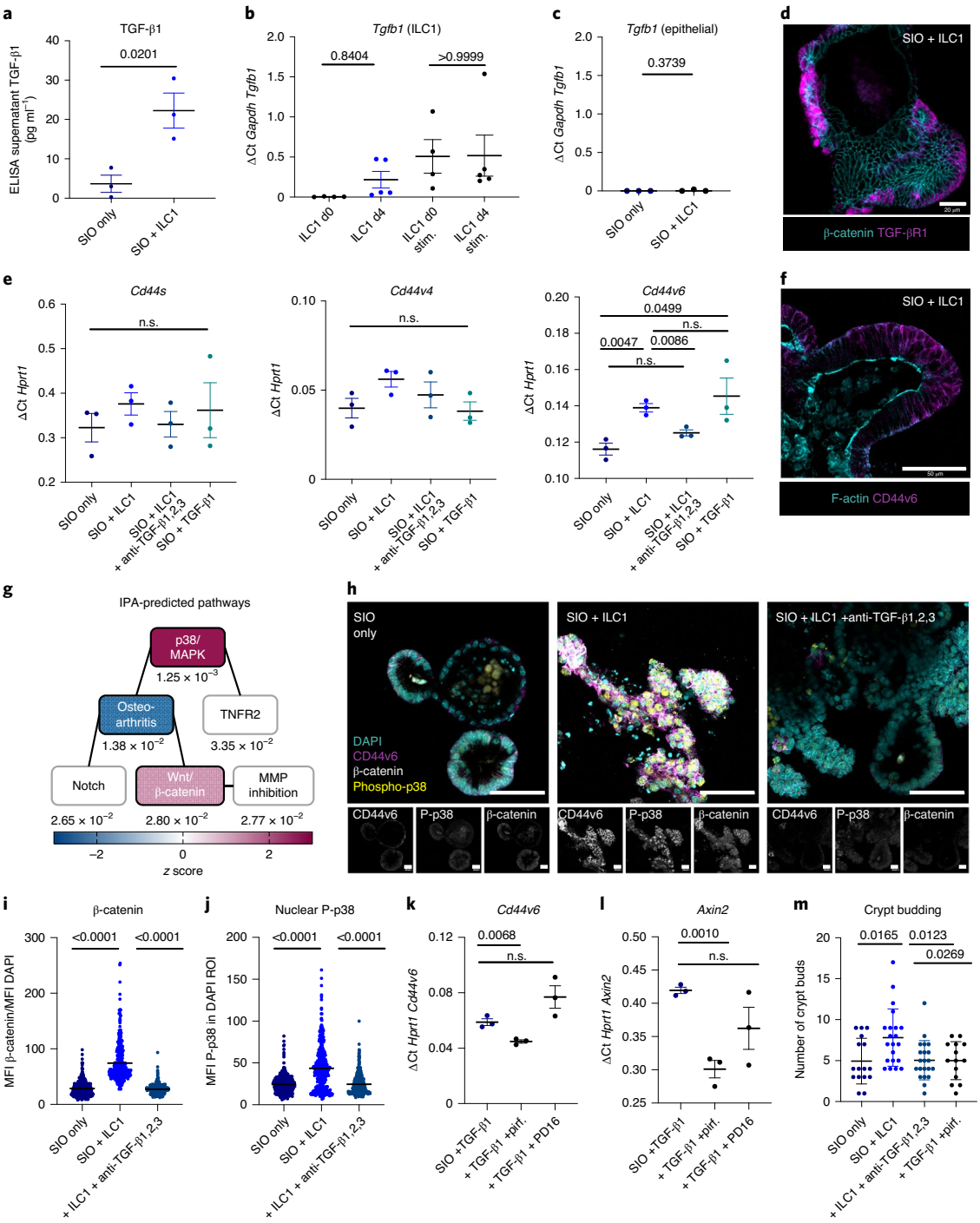

Fig. 2 | ILC1 impact epithelial crypt gene expression through TGF-β1 secretion. a, Enzyme-linked immunosorbent assay (ELISA) for latent and active TGF-β1 in culture supernatants on day 4 (ILC1 from $N=3$ mice). **b**, Expression of *Tgfb1* in primary murine ILC1 before (d0, $N=4$ mice) or after coculture (d4, cocultures derived from $N=5$ mice), with or without 2-h PMA–ionomycin activation (stim.). **c**, Expression of *Tgfb1* in IEC from SIO only or SIO + ILC1 on d4 (from $N=3$ mice). **d**, Localization of TGF-βR1 staining in SIO cocultured with ILC1 (d4) counterstained for β-catenin (representative of $N=3$). **e**, RT-qPCR with exon-specific primers for CD44 splice variants s, v4 and v6 (ILC1 derived from $N=3$ mice). **f**, Representative confocal microscopy image of CD44v6 localization in d4 SIO + ILC1, counterstained with F-actin (representative of $N=3$ mice). **g**, IPA of activated canonical pathways. Linked boxes contain overlapping differentially expressed genes (p_{adj} beneath boxes; magenta–midnight colouring represents high–low *z* score). **h**, Expression patterns of CD44v6, phosphorylated p38, β-catenin and 4,6-diamidino-2-phenylindole (DAPI) nuclei in SIO alone, with ILC1, or with ILC1 and 1-ng-ml^{-1} TGF-β1,2,3 neutralization (representative of $N=3$ mice; scale bars, 50 μm). **i**, Quantification of β-catenin accumulation in IEC of the experiment in **h**, normalized to DAPI intensity ($N=3$ mice; each symbol represents one cell; MFI, mean fluorescence intensity). **j**, Quantification of phosphorylated p38 in the DAPI+ region of the experiment in **h** (experiments from $N=3$ mice; each symbol represents one nucleus). **k**,**l**, *Cd44v6* expression (**k**) and *Axin2* expression (**l**) after 2-day culture of SIO with TGF-β1, with TGF-β1 and pirfenidone (5 μm) or with TGF-β1 and PD16 (3 μm) in $N=3$ separate experiments. **m**, Quantification of crypt budding after 4-day coculture (one-way analysis of variance (ANOVA) and Tukey test, each symbol one SIO, quantified from three experiments with ILC1 derived from $N=3$ mice). **a**–**c**,**e**,**k**,**l**, Two-tailed unpaired *t*-test; error bars, s.e.m. **i**,**j**,**m**, One-way ANOVA and Tukey test; error bars, s.e.m. (error bars are smaller than symbol size in **i**, **j**).

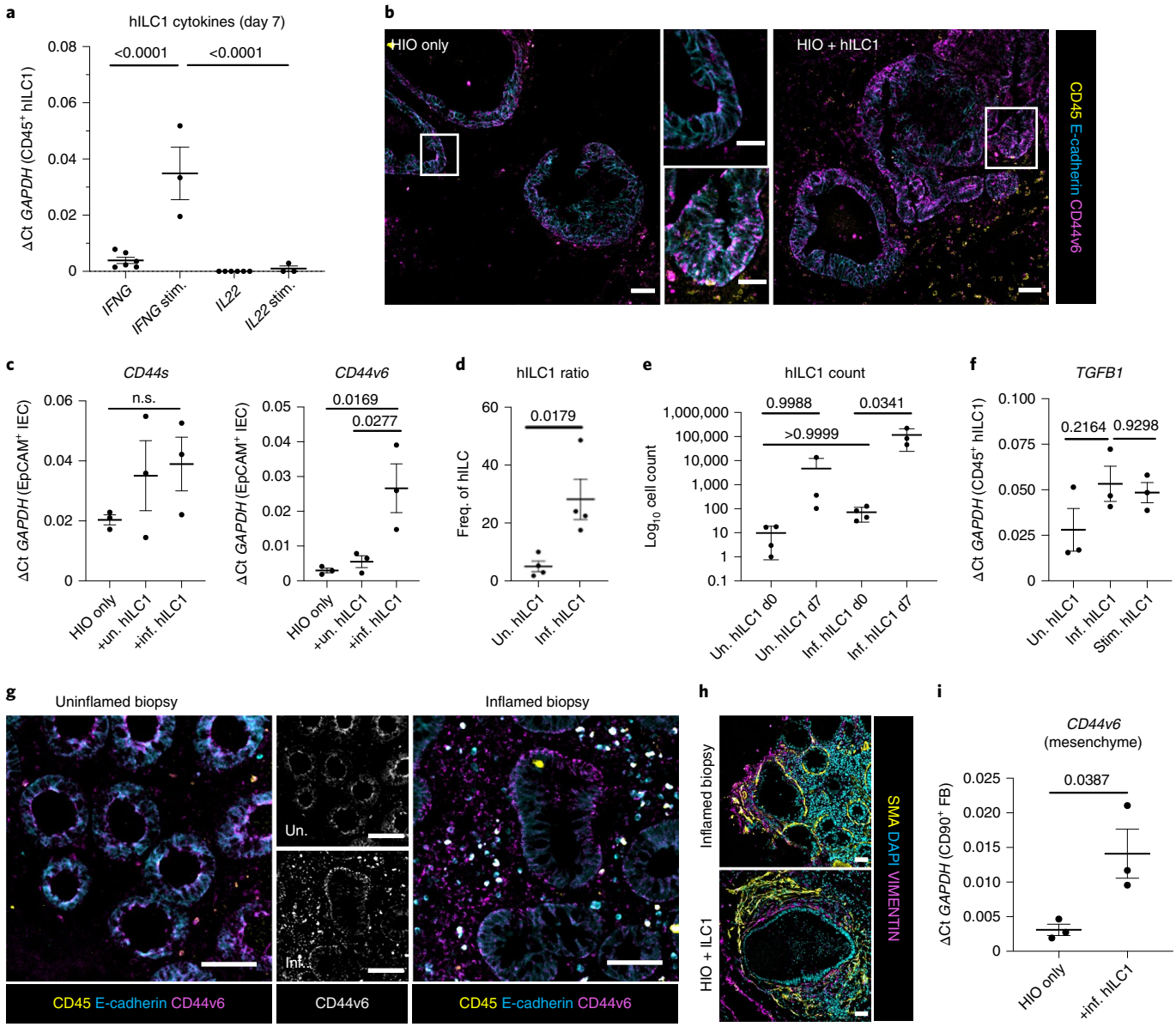

Fig. 3 | Human ILC1 drive CD44v6 expression in HIO. a, Expression of *IFNG* and *IL22* in biopsy-derived hILC1 after 7-day coculture with HIO with (ILC1 cocultures from $N=3$ patients) or without (ILC1 cocultures from $N=6$ patients) 2-h PMA–ionomycin stimulation (stim.). **b**, Corresponding representative images of E-cadherin, CD44v6 and CD45 staining of HIO cultures with or without inflamed hILC1 (scale bar, 50 µm); the white box indicates the magnified crypt (top, HIO only; bottom, HIO + hILC1; scale bar, 20 µm). **c**, Expression of *CD44s* and *CD44v6* in FACS-purified IEC from HIO only and from hILC1 coculture with inflamed (inf.) or uninflamed (un.) samples ($N=3$ patients per condition). **d**, Proportion of hILC1 relative to other Lineage$^-$CD127$^+$ ILC subtypes prior to coculture (ILC from $N=4$ uninflamed and $N=4$ inflamed tissue biopsies). **e**, Log_{10} cell count of hILC1 before (d0, from $N=4$ patients) and after (d7, from $N=3$ patients) coculture from uninflamed and inflamed biopsies. **f**, Relative expression of *TGFB1* in hILC1 from $N=3$ inflamed, $N=3$ uninflamed or $N=3$ stimulated different patients after 7-day coculture with HIO. **g**, Immunohistochemistry from biopsies from patients with IBD with or without active inflammation. CD45 lymphocytes also express E-cadherin and CD44v6. **h**, SMA$^+$ myofibroblast and VIMENTIN$^+$ fibroblast organization around the epithelium in an inflamed biopsy from a patient and in HIO + ILC1 cocultures. **i**, Relative expression of *CD44v6* in EpCAM$^-$CD45−CD90$^+$ fibroblasts (FB) purified from HIO after 7-day culture with or without inflamed hILC1 (ILC1 from $N=3$ inflamed tissue biopsies). **a**,**c**,**e**,**f**, One-way ANOVA with Tukey's test; error bars, s.e.m. **b**,**g**,**h**, Scale bars, 50 µm. **d**,**i**, Unpaired two-tailed *t*-test; error bars, s.e.m.

HIO fibroblasts expressed significantly more *CD44v6* after coculture with hILC1 from inflamed tissues (Fig. 3i), suggesting a causal link between hILC1 and mesenchymal remodelling. Since TGF-β1 is a master regulator of fibrosis, and pathological matrix remodelling is a hallmark of IBD[20], this merited further investigation.

Synthetic hydrogels enable quantification of matrix remodelling. The responsiveness of fibroblasts to hILC1 piqued our interest, as gene set enrichment analysis of the murine SIO dataset had revealed significant enrichment of ECM-remodelling genes in coculture (Supplementary Fig. 15). We also frequently observed degradation of Matrigel in murine ILC1 cocultures, which was reversible through matrix metalloproteinase (MMP) inhibition (Supplementary Fig. 16a–d). Moreover, we found that murine and human ILC1 specifically express gelatinase MMP9, a biomarker for IBD[21] (Supplementary Fig. 16e,f). Until this point, experiments

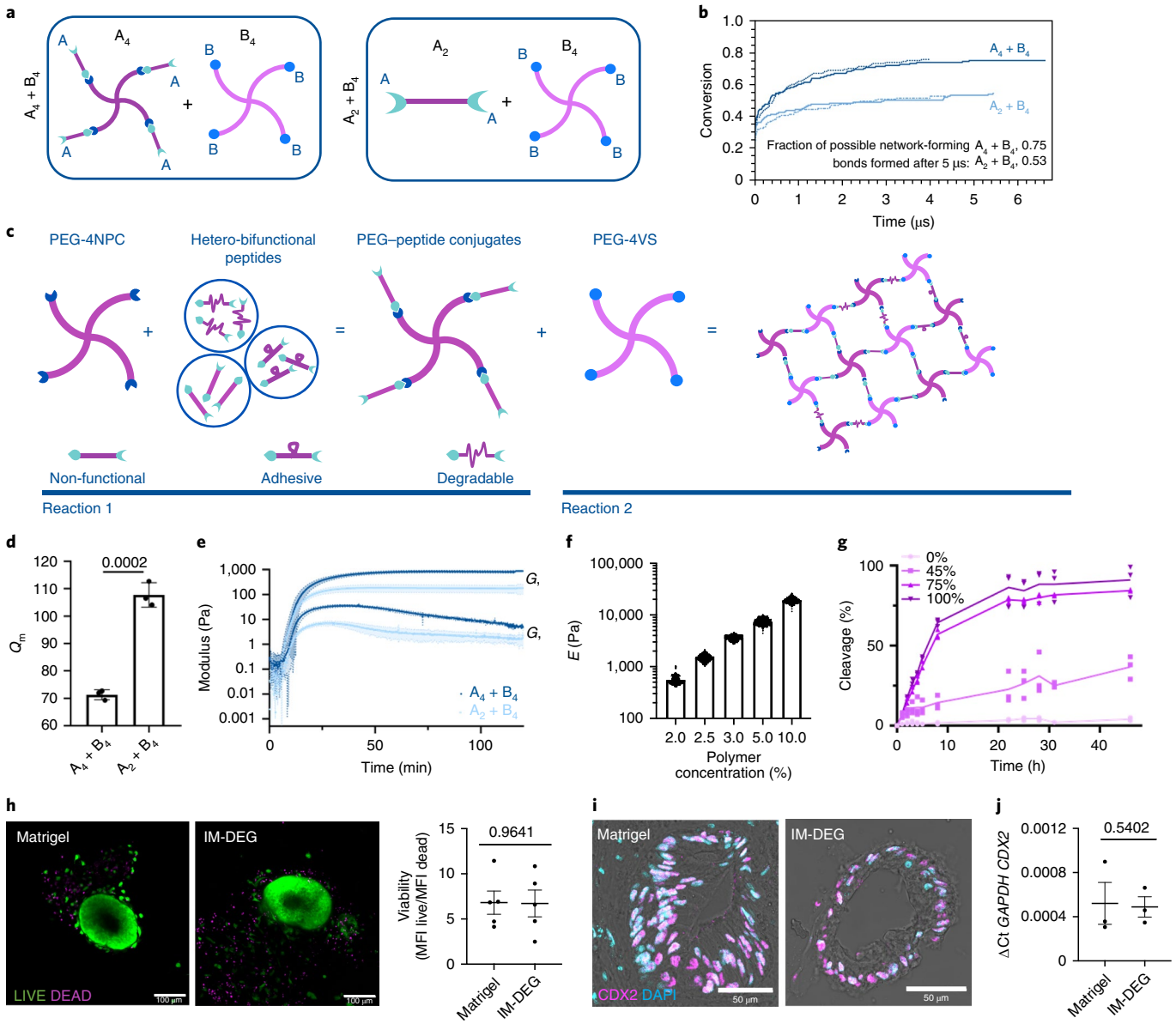

Fig. 4 | Modular PEG-based hydrogels form at low polymer concentrations and support HIO viability and phenotype. a, Molecular dynamics simulations of hydrogel crosslinking using either an A_4+B_4 or A_2+B_4 design. **b**, Plot showing fraction of total possible network-forming crosslinks formed in the molecular dynamics simulations. Lines show replicate simulations per condition. **c**, A_4+B_4 hydrogels are formed using two sequential and orthogonal click reactions. PEG-4NPC is first conjugated with degradable, adhesive or non-adhesive/non-degradable peptides, and then reacted 1:1 with PEG-4VS. Stiffness is altered by changing polymer concentration. Ligand density/degradability are controlled by varying the percentages of their respective conjugates. **d**, Mass swelling ratio (Q_m) for hydrogels formed using either A_4+B_4 or A_2+B_4 designs ($N=3$ independent hydrogels; two-tailed, unpaired *t*-test; error bars, s.d.). **e**, Rheological measurements of hydrogel formation: means and s.d. (shading) of G' and G'' obtained using time sweeps ($N=3$ independent hydrogels). **f**, *E* of hydrogels as determined by AFM-based indentation measurements ($N=3$ independent hydrogels). **g**, Percentage of crosslinking peptides cleaved over time in the presence of MMP9 for hydrogels formed with varying percentages of degradable peptide. Lines connect mean values ($N=3$ independent hydrogels). **h**, Representative images and quantification of HIO viability after 7-day encapsulation in Matrigel or IM-DEG ($N=3$ encapsulation experiments; unpaired Student *t*-test; error bars, s.e.m.). **i**,**j**, Representative images of HIO after 7-day culture in Matrigel or IM-DEG showing nuclear CDX2 localization in the epithelial monolayer (**i**), representative of $N=3$ encapsulation experiments, quantified in **j**, showing relative expression of hindgut marker *CDX2* in d75 whole HIO in Matrigel or after 7-day encapsulation in IM-DEG ($N=3$ encapsulation experiments; two-tailed, unpaired *t*-test; error bars, s.e.m.).

were conducted by resuspending cultures in three-dimensional mouse-sarcoma-derived Matrigel. This laminin-rich gel could mask or modulate matrix deposition by fibroblasts, and while it is degradable by native enzymes, the manufacturer adds proprietary concentrations of undefined MMP inhibitors[22], precluding experiments that require precise control over and quantification of matrix remodelling.

To appropriately address this question, we required a highly defined three-dimensional system with physical properties akin to those of the native intestine, but whose degradability could be independently modulated. PEG-based hydrogels with suitable stiffness have been reported, but require crosslinking by the transglutaminase Factor XIIIa[23], which is known to crosslink ECM components such as fibronectin. Fully synthetic hydrogels in which

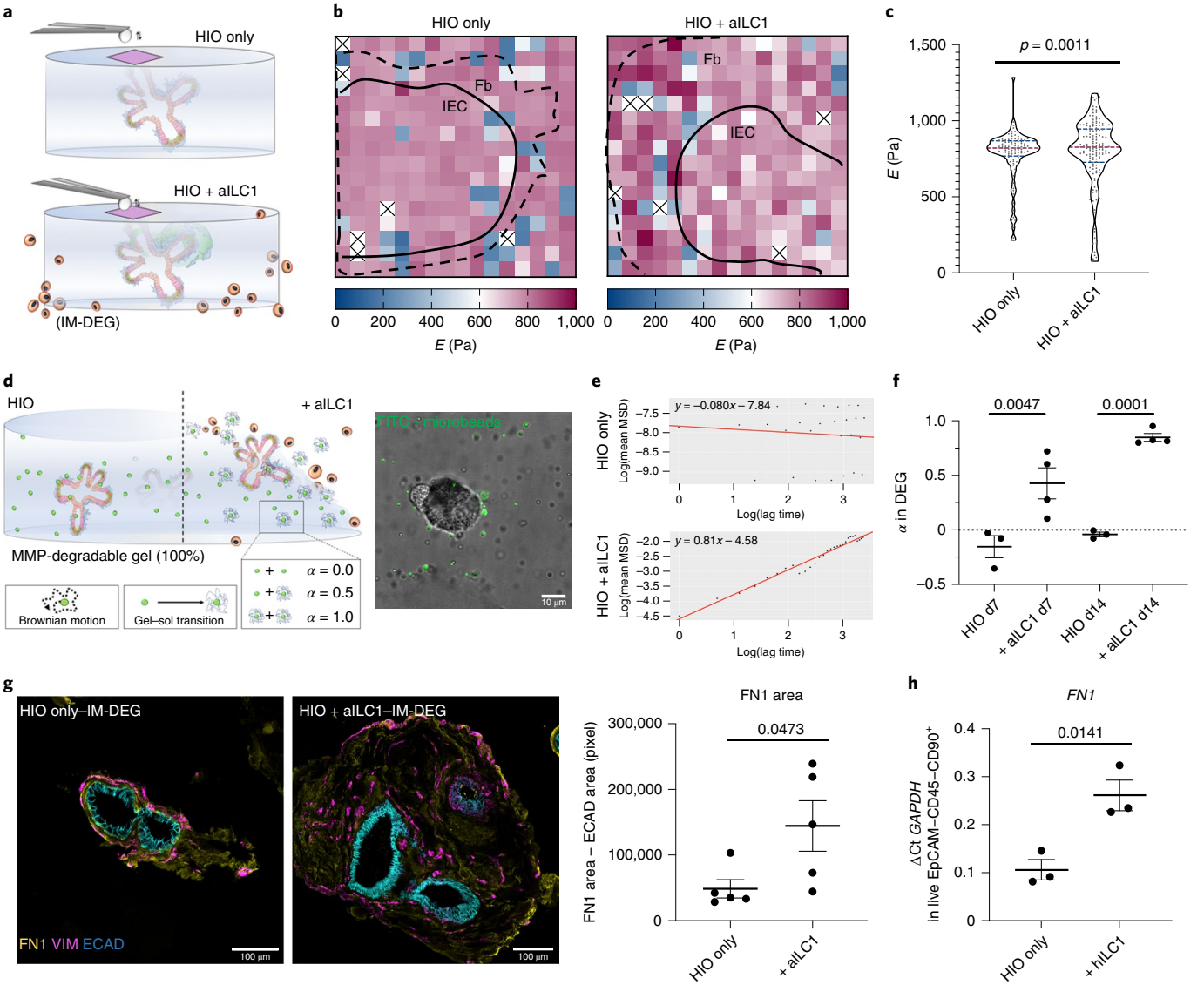

Fig. 5 | aILC1 drive HIO matrix remodelling in synthetic hydrogels. a, Schematic of AFM-based stiffness mapping strategy of HIO in IM-DEG gels, wherein the gel content (HIO) remains constant for measurements, as aILC1 from inflamed patient tissues surround the gel. **b**, Representative 150-μm × 150-μm stiffness maps of HIO-laden IM-DEG gel without (left) or with (right) aILC1, showing approximate outline of epithelial layer (IEC) and surrounding fibroblast region (Fb) based on bright-field images (Supplementary Fig. 26). White/cross squares denote omitted measurements that failed to meet quality control standards; median $E_{HIO} = 790.9$, median $E_{HIO+aILC1} = 779.9$. **c**, Violin plots summarize measurements of E on HIO-laden IM-DEG gels measured directly above organoids with or without aILC1 (approximate $p_{Kolmogorov\text{-}Smirnov} = 0.0011$, $D = 0.2525$; non-parametric Kolmogorov–Smirnov test; $N = 3$ force maps per condition; each symbol represents one force curve, magenta line indicates the median, blue lines the 25th/75th percentiles). **d**, Schematic of microrheology strategy, with corresponding sample confocal microscopy image showing distribution of fiducial fluorescein isothiocyanate (FITC) beads within an HIO-laden, fully degradable gel (scale bar, 10 μm; representative of $N = 4$ encapsulation experiments). α is the logarithmic slope of a bead's mean-squared displacement and is an indicator of bead motion (1, Brownian motion; 0, immobile; α transitions from 0 to 1 as the local hydrogel undergoes a gel–sol transition). **e**, Representative plots generated in R showing α for HIO only (top) and HIO + aILC1 (bottom). **f**, α for HIO encapsulated in 100% DEG gels after 7 and 14 days with or without aILC1 ($N = 4$ encapsulation experiments). **g**, Representative staining of fibronectin 1 deposition and VIMENTIN$^+$ fibroblasts in HIO with or without aILC1 (maximum projection 10 z stacks) with quantification of FN1$^+$ area normalized to ECAD$^+$ area ($N = 5$ separate organoid areas). **h**, Expression of *FN1* in EpCAM$^-$CD45$^-$CD90$^+$ fibroblasts after 7-day culture with or without inflamed hILC1 (ILC1 derived from $N = 3$ patients). **f**,**g**, Unpaired two-tailed Student t-test; **h**, one-way ANOVA with Tukey's test; error bars, s.e.m.

homo-bifunctional peptides (A_2) act as crosslinkers of four- or eight-arm PEGs (B_4/B_8) have also been described; however, when crosslinkers bear two identical functional groups that react indiscriminately towards the chain end of any PEG arm, primary loop formation[24] can impact network connectivity. This is critical when forming soft, tissue-like hydrogels that require low polymer concentrations, resulting in slow and inefficient network formation in which organoids reach the tissue culture plastic beneath the hydrogel prior to three-dimensional gelation[25].

$A_4 + B_4$ hydrogel designs that avoid primary looping could yield more effectively crosslinked networks than $A_2 + B_4$ systems[26] (Fig. 4a). To explore if this held true at low polymer concentrations, we carried out coarse-grained molecular dynamics simulations. Molecular dynamics simulations use classical laws of mechanics

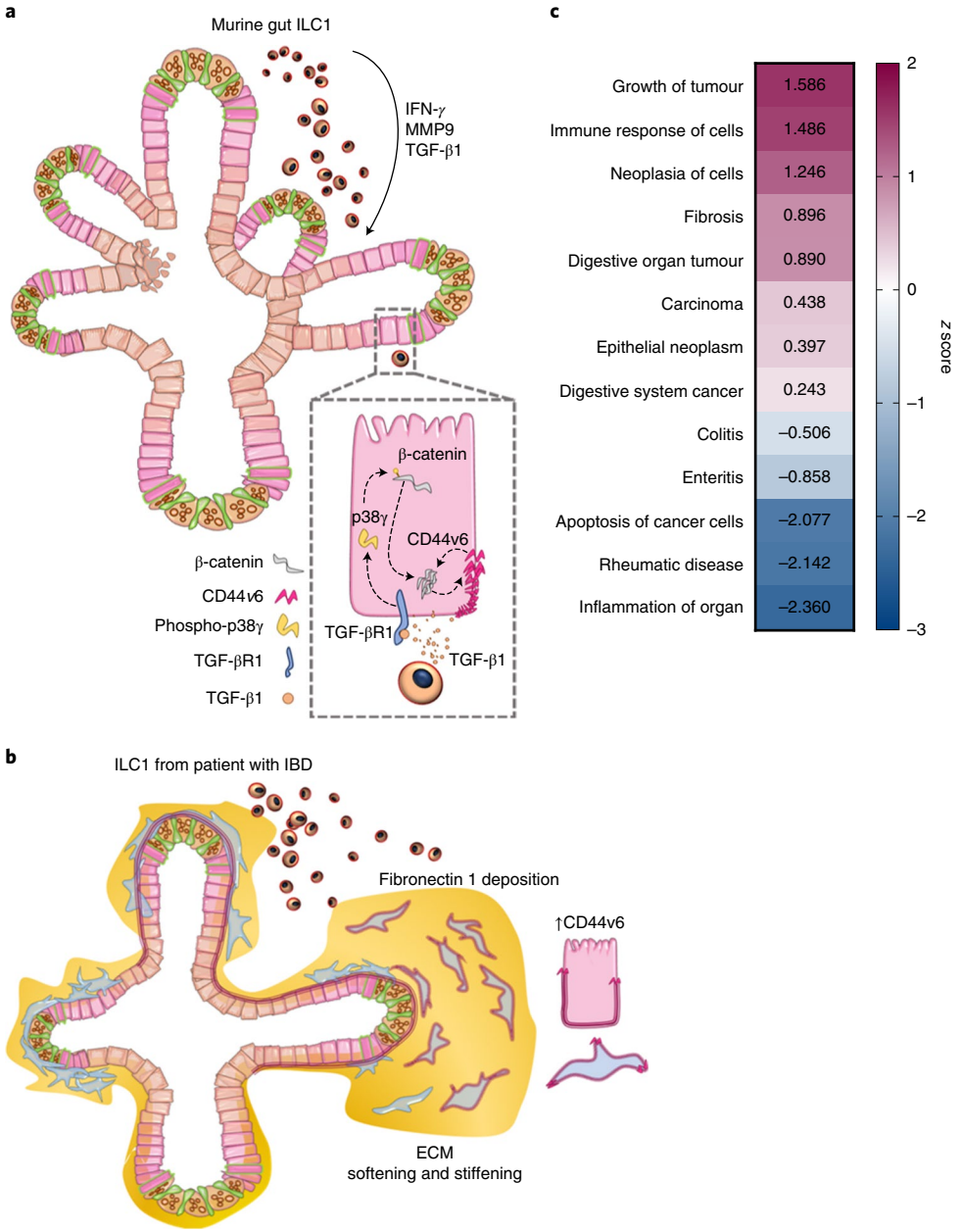

Fig. 6 | Overview of proposed impact of ILC1 on gut organoids. a, Murine ILC1 drive epithelial crypt budding in SIO through TGF-β1-induced phosphorylation of p38γ, which drives β-catenin accumulation and expression of *Axin2* and *CD44v6*. We propose that CD44v6 and β-catenin might engage in a positive feedback loop, driving epithelial-subtype-non-specific proliferation. **b**, hILC1 derived from patients with IBD express *TGFB1* and *MMP9*. ILC1 isolated from tissues with active inflammation also drive expression of both epithelial and mesenchymal CD44v6 in HIO. Moreover, these patient-derived ILC1 drive increased deposition of fibronectin 1 and MMP-mediated matrix degradation, resulting in a balance of matrix softening and stiffening. **c**, IPA of the murine RNA-seq dataset showing cumulative gene enrichment (*z* score) in SIO cocultured with ILC1 indicative of activation (magenta) and inhibition (blue) of selected gastrointestinal and inflammatory diseases and function (ILC1 derived from $N=3$ mice).

to provide insight into probable molecular arrangements within a material. Simulations showed that A_4+B_4 designs facilitated the formation of more network-forming crosslinks than A_2+B_4 designs, in which ~25% of crosslinks were primary loops (Fig. 4b and Supplementary Figs. 17 and 18).

To create an A_4+B_4 design, we formed hydrogels using two sequential click reactions in which all peptides acted as crosslinkers (Fig. 4c and Supplementary Fig. 19). First, the amine side group of a single lysine placed close to the peptides' amino-terminus was reacted with star-shaped, four-arm PEG activated at each terminus with nitrophenyl carbonate (PEG-4NPC) (A_4), yielding PEG–peptide conjugates (conjugation efficiency 81–91%). Hydrogels were then formed through a Michael addition between a carboxy-terminal free thiol and the end terminus of star-shaped four-arm PEG (20 kDa, unless otherwise noted) bearing vinyl sulfone groups at each chain terminus (PEG-4VS) (B_4) (>90% efficiency) (Supplementary Fig. 20). A_4+B_4 hydrogels had more effectively crosslinked networks with lower swelling ratios (Fig. 4d), which were both stiffer and behaved more elastically (Fig. 4e and Supplementary Fig. 21) than A_2+B_4 designs formed using homo-bifunctional peptides. Moreover, although A_4+B_4 hydrogels abandoned standard pendant presentations of adhesive ligands,

human mesenchymal stromal cells could still adhere to their surfaces (Supplementary Fig. 22). Young's modulus (E) of A_4+B_4 hydrogels could be varied by modulating polymer concentration (Fig. 4f) to achieve values for E similar to that of normal human intestinal tissue (750–1,250 Pa) (ref. [27]), and were susceptible to degradation by MMP9 (Fig. 4g). Taken together, these results suggest suitable properties to explore HIO matrix remodelling.

Human ILC1 drive matrix remodelling. Equipped with an appropriate culture system, we found that HIO encapsulated in degradable (DEG), non-degradable (NON-DEG) and intermediately degradable (IM-DEG, 45% MMP-cleavable peptides) hydrogels were viable (Fig. 4h and Supplementary Fig. 23), and maintained their characteristic phenotype, as in Matrigel (Fig. 4i,j and Supplementary Fig. 24a,b). Moreover, HIO fibroblasts were capable of depositing native ECM in this system, which also did not alter CD44 expression (Supplementary Fig. 25b–d). We then harnessed this system to quantitatively dissect the impact of hILC1 on the physical properties of HIO–hydrogel cultures.

First, we used atomic force microscopy (AFM)-based indentation to map cell-mediated changes in stiffness. Since phenotypically irrelevant differences in mechanical properties between conditions could arise from the physical presence of hILC1 within the gel, we opted to surround the HIO-laden hydrogels with ancillary hILC1 from inflamed biopsies (aILC1), keeping the composition of the microenvironment that we mapped constant (Fig. 5a). We collected force–distance measurements using a bead-functionalized cantilever (Supplementary Fig. 26), and observed increased heterogeneity of E across maps with aILC1 (Fig. 5b). Indeed, we saw a significant difference in variance of E induced by coculture with aILC1 ($F=0.0004$; $p_{\text{Kolmogorov-Smirnov}}=0.0011$) (Fig. 5c). Since aILC1 appeared to induce both stiffening and softening of the matrix, while median E remained comparable between samples, this could suggest a balance between cell-mediated matrix production and degradation.

To ensure that aILC1 had the same capacity to degrade engineered hydrogels as Matrigel, we next performed multiple-particle-tracking microrheology, monitoring the Brownian motion of fluorescent fiducial beads distributed within the hydrogel (Fig. 5d). Beads are capable of moving within DEG hydrogels (100% MMP-cleavable peptides) when enzyme-mediated degradation causes a sufficient portion of their local environment to undergo a gel–sol transition, prompting the logarithmic slope of a bead's mean-squared displacement, α, to transition from 0 to 1 (ref. [28]) (Fig. 5e). After 7 days, aILC1 coculture significantly increased α relative to HIO-only controls (Fig. 5f), with near-complete degradation after 2 weeks ($\alpha=0.847$). While the 55% non-degradable IM-DEG gel used for AFM was explicitly designed to not undergo a gel–sol transition, this microrheological quantification of aILC1's capacity to degrade a 100% MMP-sensitive system provides explanation for the softening recorded by AFM, which is sensitive to subtle changes in the stiffness of ~1 kPa hydrogels.

Next, we assessed how ILC1 might contribute to hydrogel stiffening observed in fibroblast-rich, peri-organoid regions. We observed that aILC1 drove a significant increase in the area of peri-organoid FN1 deposition (Fig. 5g and Supplementary Fig. 27). This phenotype was recapitulated in Matrigel, where aILC1 increased expression of *FN1* and *COL1a1* in HIO-derived fibroblasts (Fig. 5h and Supplementary Fig. 28a), and increased FN1 deposition, which was recapitulated with recombinant TGF-β1 (Supplementary Fig. 28b). Specific upregulation of fibronectin 1 is consistent with non-canonical, SMAD-independent TGF-β1 signalling via Jun/p38, which drives *FN1* expression[29]. We therefore suggest that a balance between ILC1-derived MMP degradation and ILC1-induced mesenchymal ECM deposition accounts for the quantitative difference in coefficient of variance captured in the AFM stiffness maps.

In summary, our A_4+B_4 defined hydrogel allowed us to conclusively assess that hILC1 drive ECM remodelling in the intestine.

Discussion

Here, we have identified murine ILC1 as an important source of TGF-β1, which promotes CD44v6$^+$ epithelial crypt growth through p38γ-induced proliferation (Fig. 6a). ILC1 isolated from patients with IBD and active inflammation and recombinant TGF-β1 also drove upregulation of CD44v6 in epithelial and mesenchymal cells. To more thoroughly investigate this role of hILC1 in mesenchymal remodelling emerging from our data, we then developed a highly defined synthetic hydrogel system, which allowed us to quantify hILC1-mediated matrix degradation and stiffening. The introduction of TGF-β1 and MMP9 as a part of the ILC1 inflammatory response is in line with a recently published RNA-seq dataset of human ILC1, which showed increased expression of *TGFB1* and *MMP9* in patients with an acute risk of myocardial infarction relative to healthy controls[30].

Speculation about the impact of TGF-β1 in the context of the gastrointestinal immune system is a complex task, as the microbiome, the enteric nervous system and other immune cells differentially respond to this pleiotropic cytokine. For instance, while TGF-β1 is a master regulator of fibrosis in fibroblasts[31], it is anti-inflammatory in the adaptive immune system[32], and can regulate plasticity between the ILC subsets[33]. We observed expression of TGF-β1 in tandem with IFN-γ, suggesting that these cytokines may act in concert, and highlighting the importance of our dataset being derived from cocultures with ILC1, not recombinant cytokines. Moreover, despite the presence of IFN-γ in our system, pathway analysis predicted a decrease in inflammatory phenotypes, but an increase in epithelial gene signatures consistent with tumour growth and fibrosis (Fig. 6b). This fits with the pathogenic association of splice variant CD44v6, which exacerbates aggressive ovarian cancer by driving β-catenin expression[34], driving intestinal cancer initiation[35], progression[9,36] and metastasis[37] in these tissues. Moreover, fibrotic fibronectin deposition correlates with resistance to anti-TNF-α treatment in patients with Crohn's disease[38]. Thus, our findings suggest that, while ILC1 may have an unexpected anti-inflammatory role in the gut, their accumulation in inflamed tissues could exacerbate IBD-associated comorbidities, and could be an indicator for poor treatment response. This unexpected contextualization of intestinal ILC1 was enabled by our reductionist, modular and synthetic culture system, which could be further exploited to dissect dynamic interactions between other inaccessible cells and tissues, in both development and disease.

Online content

Any methods, additional references, Nature Research reporting summaries, source data, extended data, supplementary information, acknowledgements, peer review information; details of author contributions and competing interests; and statements of data and code availability are available at https://doi.org/10.1038/s41563-020-0783-8.

Received: 30 June 2019; Accepted: 23 July 2020;
Published online: 7 September 2020

References

1. Haber, A. L. et al. A single-cell survey of the small intestinal epithelium. *Nature* **551**, 333–339 (2017).
2. Vivier, E. et al. Innate lymphoid cells: 10 years on. *Cell* **174**, 1054–1066 (2018).
3. Lindemans, C. et al. Interleukin-22 promotes intestinal-stem-cell-mediated epithelial regeneration. *Nature* **528**, 560 (2015).
4. Spits, H., Bernink, J. H. & Lanier, L. NK cells and type 1 innate lymphoid cells: partners in host defense. *Nat. Immunol.* **17**, 758–764 (2016).
5. Bernink, J. H. et al. Human type 1 innate lymphoid cells accumulate in inflamed mucosal tissues. *Nat. Immunol.* **14**, 221–229 (2013).

6. Pagnini, C., Pizarro, T. T. & Cominelli, F. Novel pharmacological therapy in inflammatory bowel diseases: beyond anti-tumor necrosis factor. *Front. Pharmacol.* **10**, 671 (2019).
7. Sato, T. et al. Paneth cells constitute the niche for Lgr5 stem cells in intestinal crypts. *Nature* **469**, 415–418 (2011).
8. Spence, J. R. et al. Directed differentiation of human pluripotent stem cells into intestinal tissue in vitro. *Nature* **470**, 105–109 (2011).
9. Senbanjo, L. T. & Chellaiah, M. A. CD44: a multifunctional cell surface adhesion receptor is a regulator of progression and metastasis of cancer cells. *Front. Cell Dev. Biol.* **5**, 18 (2017).
10. Martin-Gallausiaux, C. et al. Butyrate produced by gut commensal bacteria activates TGF-beta1 expression through the transcription factor SP1 in human intestinal epithelial cells. *Sci. Rep.* **8**, 9742 (2018).
11. Zeilstra, J. et al. Stem cell CD44v isoforms promote intestinal cancer formation in Apc(min) mice downstream of Wnt signaling. *Oncogene* **33**, 665–670 (2014).
12. Ghatak, S. et al. Transforming growth factor β1 (TGFβ1) regulates CD44V6 expression and activity through extracellular signal-regulated kinase (ERK)-induced EGR1 in pulmonary fibrogenic fibroblasts. *J. Biol. Chem.* **292**, 10465–10489 (2017).
13. Schmitt, M., Metzger, M., Gradl, D., Davidson, G. & Orian-Rousseau, V. CD44 functions in Wnt signaling by regulating LRP6 localization and activation. *Cell Death Differ.* **22**, 677–689 (2015).
14. Ribes, B. M. et al. Effectiveness and safety of pirfenidone for idiopathic pulmonary fibrosis. *Eur. J. Hosp. Pharm.* https://doi.org/10.1136/ejhpharm-2018-001806 (2019).
15. Yin, N. et al. p38γ MAPK is required for inflammation-associated colon tumorigenesis. *Oncogene* **35**, 1039–1048 (2016).
16. Fujii, M. et al. Human intestinal organoids maintain self-renewal capacity and cellular diversity in niche-inspired culture condition. *Cell Stem Cell* **23**, 787–793.e6 (2018).
17. Dotti, I. et al. Alterations in the epithelial stem cell compartment could contribute to permanent changes in the mucosa of patients with ulcerative colitis. *Gut* **66**, 2069–2079 (2017).
18. McCracken, K. W., Howell, J. C., Wells, J. M. & Spence, J. R. Generating human intestinal tissue from pluripotent stem cells in vitro. *Nat. Protoc.* **6**, 1920–1928 (2011).
19. Jung, K. B. et al. Interleukin-2 induces the in vitro maturation of human pluripotent stem cell-derived intestinal organoids. *Nat. Commun.* **9**, 3039 (2018).
20. Shimshoni, E., Yablecovitch, D., Baram, L., Dotan, I. & Sagi, I. ECM remodelling in IBD: innocent bystander or partner in crime? The emerging role of extracellular molecular events in sustaining intestinal inflammation. *Gut* **64**, 367–372 (2015).
21. Farkas, K. et al. The diagnostic value of a new fecal marker, matrix metalloprotease-9, in different types of inflammatory bowel diseases. *J. Crohn's Colitis* **9**, 231–237 (2015).
22. Hughes, C. S., Postovit, L. M. & Lajoie, G. A. Matrigel: a complex protein mixture required for optimal growth of cell culture. *Proteomics* **10**, 1886–1890 (2010).
23. Ehrbar, M. et al. Biomolecular hydrogels formed and degraded via site-specific enzymatic reactions. *Biomacromolecules* **8**, 3000–3007 (2007).
24. Zhong, M., Wang, R., Kawamoto, K., Olsen, B. D. & Johnson, J. A. Quantifying the impact of molecular defects on polymer network elasticity. *Science* **353**, 1264–1268 (2016).
25. Cruz-Acuña, R. et al. PEG-4MAL hydrogels for human organoid generation, culture, and in vivo delivery. *Nat. Protoc.* **13**, 2102–2119 (2018).
26. Gu, Y. et al. Semibatch monomer addition as a general method to tune and enhance the mechanics of polymer networks via loop-defect control. *Proc. Natl Acad. Sci. USA* **114**, 4875–4880 (2017).
27. Stewart, D. C. et al. Quantitative assessment of intestinal stiffness and associations with fibrosis in human inflammatory bowel disease. *PLoS ONE* **13**, e0200377 (2018).
28. Schultz, K. M., Kyburz, K. A. & Anseth, K. S. Measuring dynamic cell–material interactions and remodeling during 3D human mesenchymal stem cell migration in hydrogels. *Proc. Natl Acad. Sci. USA* **112**, E3757–E3764 (2015).
29. Hocevar, B. A., Brown, T. L. & Howe, P. H. TGF-beta induces fibronectin synthesis through a c-Jun N-terminal kinase-dependent, Smad4-independent pathway. *EMBO J.* **18**, 1345–1356 (1999).
30. Li, J., Wu, J., Zhang, M. & Zheng, Y. Dynamic changes of innate lymphoid cells in acute ST-segment elevation myocardial infarction and its association with clinical outcomes. *Sci. Rep.* **10**, 5099 (2020).
31. Bauché, D. & Marie, J. C. Transforming growth factor β: a master regulator of the gut microbiota and immune cell interactions. *Clin. Transl. Immunol.* **6**, e136 (2017).
32. Fenton, T. M. et al. Inflammatory cues enhance TGFβ activation by distinct subsets of human intestinal dendritic cells via integrin αvβ8. *Mucosal Immunol.* **10**, 624–634 (2017).
33. Bal, S. M., Golebski, K. & Spits, H. Plasticity of innate lymphoid cell subsets. *Nat. Rev. Immunol.* https://doi.org/10.1038/s41577-020-0282-9 (2020).
34. Wang, J. et al. CD44v6 promotes β-catenin and TGF-β expression, inducing aggression in ovarian cancer cells. *Mol. Med Rep.* **11**, 3505–3510 (2015).
35. Wang, Z., Zhao, K., Hackert, T. & Zöller, M. CD44/CD44v6 a reliable companion in cancer-initiating cell maintenance and tumor progression. *Front. Cell Dev. Biol.* **6**, 97 (2018).
36. Ma, L., Dong, L. & Chang, P. CD44v6 engages in colorectal cancer progression. *Cell Death Dis.* **10**, 30 (2019).
37. Todaro, M. et al. CD44v6 is a marker of constitutive and reprogrammed cancer stem cells driving colon cancer metastasis. *Cell Stem Cell* **14**, 342–356 (2014).
38. de Bruyn, J. R. et al. Intestinal fibrosis is associated with lack of response to Infliximab therapy in Crohn's disease. *PLoS ONE* **13**, e0190999 (2018).

Methods

Establishment of murine SIO cultures. Organoid cultures were established by isolating intact small-intestine crypts from 6–8-week female CD45.1 C57BL/6 mice following established protocols[39] and propagated in Matrigel (Corning) in basal medium (DMEM/F12, 2-mM GlutaMAX, 10-mM HEPES, 1× antibiotic–antimycotic, 1× N-2 supplement, 1× B-27 supplement, all Thermo Fisher; 1-mM acetyl-L-cysteine, Sigma) supplemented with epidermal growth factor (50 ng ml^{-1}, R&D) and 50 µl ml^{-1} of supernatant from both R-spondin (RSpo1-Fc) and Noggin cell lines, passaged every 4–5 days. The RSpo1-Fc cell line was a gift from C. Kuo (Stanford University, USA) and the Noggin cell line was a gift from the Hubrecht Institute.

Murine intestinal lymphocyte isolation. Lamina propria ILC1 were isolated from small intestines of litter-matched female RORγt–GFP (green fluorescent protein) reporter mice following established protocols[40]. In short, excess fat and Peyer's patches were removed from the intestine, which was then opened longitudinally and rinsed thoroughly in ice-cold PBS. Small (1-cm) sections were incubated in epithelial cell removal buffer for 2 × 15 min (5-mM EDTA and 10-mM HEPES in Hanks' balanced salt solution (HBSS), Gibco), then tissue was cut into small pieces for extensive digestion of the ECM (collagenase (500 µg ml^{-1}), dispase (0.5 U ml^{-1}), DNase1 (500 µg ml^{-1}), 2% fetal bovine serum (FBS) in HBSS, Gibco). Samples were filtered through a 40-µm strainer in 10% FBS–DMEM10, then lymphocytes were isolated using an 80%/40% isotonic Percoll density gradient separation (centrifuged at 900 *g* for 25 min, no breaks on acceleration or deceleration). The interphase between 40% and 80% Percoll was collected, filtered and prepared for FACS isolation of ILC1 without further enrichment. Next, lymphocytes were rinsed with PBS, then stained with fixable LIVE/DEAD ultraviolet (Thermo Fisher) in PBS for 15 min in the dark at 4 °C. The dye was quenched with sorting buffer, then the Fc receptor was blocked with anti-CD16/CD32, clone 93, for 10 min at 4 °C, followed by extracellular staining following standard flow cytometry protocols (1 µl antibody/100 µl sorting buffer/5 million cells unless otherwise indicated). FACS antibodies were sourced from eBioscience (with the exception of CD45) and were as follows: CD3–Fluor450 (RB6-8C5), CD5–Fluor450 (53-7.3), CD19–Fluor450 (eBio1D3), Ly6G–Fluor450 (RB6-8C5), CD45–BV510 (30-F11, BioLegend) CD127–APC (A7R34), KLRG1–PerCP/eFluor710 (2F1), NKp46–PE/Cyanine7 (29A1.4) and NK1.1–PE (PK136). Cells were rinsed, and sorted on a 70-µm nozzle after calculation of compensation and acquisition of fluorescence minus one controls for Lineage, CD127 and NKp46. Gating strategies are outlined in Supplementary Figures.

Murine ILC–organoid cocultures. Approximately 1,500–2,500 murine ILC1 were seeded with ~100 mechanically disrupted SIO crypts per well, resuspended in 30 µl ice-cold Matrigel, pipetted onto preheated tissue culture plates (Nunclon) and incubated at 37 °C for 15–20 min prior to addition of prewarmed basal medium supplemented with 50-mM B2ME (R&D), 20-ng-ml^{-1} rhIL-2 (Sigma), 20-ng-ml^{-1} rmIL-7 (R&D) and 1-ng-ml^{-1} IL-15 (R&D), with medium changes every 2–4 days.

Human iPSC-derived intestinal organoids. The healthy KUTE-4 female skin-fibroblast-derived human iPSC (hiPSC) line (available from the European Collection of Authenticated Cell Cultures, karyotyped, passages 24–36) was cultured on plates coated with 40-µl-ml^{-1} vitronectin in PBS (STEMCELL Technologies). E8 (Gibco) medium was changed daily, pockets of differentiation were actively removed, and round, pluripotent colonies were passaged with EDTA (Versene, Gibco) every 4–6 days, when 60–70% confluent or before circular colonies began merging.

KUTE-4 hiPSC were differentiated into HIO following established protocols[18]. In short, hiPSC were patterned toward definitive endoderm in Roswell Park Memorial Institute medium (RPMI) with daily increasing B-27 (0.2%, 1%, 2%) and 100-ng-ml^{-1} activin A (R&D) for 3.5 days, then patterned towards midgut in RPMI + 2% B-27 with 3-µM CHIR99021 (Wnt agonist, TOCRIS) and 500-ng-ml^{-1} recombinant fibroblast growth factor 4 (R&D) for 4 days. At this point, CDX2 colonies were picked using a 200-µl pipette tip, replated in 35 µl Matrigel, then matured in basal medium with human epidermal growth factor (100 ng ml^{-1}, R&D), rh-R-spondin (500 ng ml^{-1}, R&D), rh-Noggin (100 ng ml^{-1}, R&D) and 2-ng-ml^{-1} IL-2 supernatant for at least 35 days prior to establishing cocultures with hILC1 or encapsulation in synthetic hydrogels for aILC1 characterization.

Human lymphocyte isolation from patient biopsies. Studies in human tissues received ethical approval from the London Dulwich Research Ethics Committee (reference 15/LO/1998). Informed written consent was obtained in all cases. Inflammatory status of patients with IBD was diagnosed by a consultant, and up to 12 colonic biopsies were procured by endoscopy. These were cultured on rat tail collagen-I-coated 9-mm × 9-mm × 1.5-mm Cellfoam matrices (Cytomatrix) in complete medium (RPMI with 10% fetal bovine serum) with antibiotics (penicillin, streptomycin, metronidazole, gentamicin and amphotericin) for 48 h following established protocols[41,42]. Colonic lamina propria mononuclear cells (cLPMCs) were then isolated from the supernatant ready for evaluation (protocol adapted from ref. [41]). Then, cLPMC were rinsed with PBS, treated with fixable LIVE/DEAD ultraviolet and Fc blocked before being stained with CD45–eFluor450 (HI30; Invitrogen), Lineage cocktail 3–FITC (CD3, CD14, CD19, CD20; BD Biosciences), CD4–FITC (OKT4; BioLegend), T-cell antigen receptor (TCR)-α/β–FITC (IP26; BioLegend), TCR-γ/δ–FITC (B1; BioLegend), CD56–Alexa700 (B159; BD Pharmingen), CD7–PE–CF594 (M-T701; BD Horizon), CD127–PE–Cy7 (eBioRDR5; Invitrogen), c-Kit–BV605 (104D2; BioLegend), CRTH2–PE (MACS; Miltenyi Biotec) and CD161–APC (HP-3G10; BioLegend). cLPMC were sorted on a 70-µM nozzle on an Aria 2 (BD) using BD FACS Diva 8.0.1 software. One biopsy per patient was fixed in 4% paraformaldehyde and maintained for histology.

Human ILC1–organoid cocultures. Approximately 15–30 mature HIO were added to Eppendorf tubes containing 50–300 hILC1 directly after FACS isolation from biopsies. The two components were centrifuged at 500 *g* for 3 min, supernatant was carefully removed, and the cocultures were resuspended in 35 µl Matrigel and plated onto prewarmed tissue culture treated plates. The same culture conditions as optimized for murine cocultures were used for HIO–hILC1 cocultures, including 50-mM B2ME (R&D), 20-ng-ml^{-1} rhIL-2 (Sigma), 20-ng-ml^{-1} rmIL-7 (R&D) and 1-ng-ml^{-1} IL-15 (R&D), with medium changes every 3–4 days.

Cell isolation from cocultures. After 4 days of murine and 7 days of human coculture, Matrigel was disrupted and cells were collected into 15-ml Falcon tubes. For murine ILC1 cultures Matrigel disruption was not required, and cells were gently rinsed from the bottom of the plate using PBS + 2% FBS. Samples were rinsed with PBS, then dissociated in TrypLE (Gibco) for 20 min at 37 °C. The sorting buffer after this step contained DNase (250 µg ml^{-1}), EDTA (1 µl ml^{-1}) and HEPES (1 µl ml^{-1}) to maintain single epithelial cells and avoid clumping. Single cells were centrifuged and resuspended in sorting buffer. Cells were then filtered (70 µm), having precoated the filter with sorting buffer to minimize cell loss, and either rinsed with PBS for fixable LIVE/DEAD staining (ultraviolet or near-infrared, Thermo Fisher), or stained with EpCAM, CD45 and the requisite combination of antibodies for the experiment, and analysed (BD Fortessa) or sorted (BD ARIA3 Fusion and BD Aria 2 using BD FACS Diva 8.0.1 software). Isolation of murine IEC and ILC1 following coculture was performed using EpCAM–APC Cy7 (G8.8, BioLegend), CD45–BV510 (30-F11, BioLegend), NK1.1 BV605 (PK136, BioLegend) and CD44–PE (IM7, BioLegend). Isolation of human IEC, fibroblasts and hILC1 used fixable LIVE/DEAD ultraviolet or LIVE/DEAD near-infrared CD45–eFluor450 (HI30, Invitrogen), EpCAM–FITC (9C4, BioLegend) and CD90–PE/Dazzle (Thy1, BioLegend).

Flow cytometry. Flow cytometry data were acquired on a BD Fortessa2 and analysed using FlowJo v10.5.3.

RT–qPCR. For RNA isolation, cells were FACSed directly into 250 µl RLT (QIAGEN) lysis buffer supplemented with 10-µl-ml^{-1} β-mercaptoethanol to stabilize the RNAse-rich intestinal epithelial tissue lysate. RNA was isolated using an RNeasy MicroRNA isolation kit (QIAGEN), and complementary DNA produced using RevertAid (Fisher), using oligo-dTTTTT primers. RT–qPCR based on Fast SYBR Green Mix (Applied Biosystems) was run on a CFX384 Touch real-time PCR detection system (Bio-Rad), with no-template controls and melting curves for quality control, or using TaqMan Gene Expression Master Mix (Applied Biosystems) with fluorescein amidite probes, using an annealing temperature of 60 °C for 39 cycles. All kits were used following manufacturers' instructions. Primers were designed using PrimerBank and verified via BLAST against the *Mus musculus* or *Homo sapiens* genome on ensemble.org. ΔCq values were normalized to the housekeeping genes *Hprt1* or *GAPDH* for SYBR and *HPRT1* for TAQ probes. All primers are listed in Supplementary Table 1.

Cytokine quantification. TGF-β1 concentration in supernatant from 4-day ILC1 cocultures and SIO-only controls was measured using the mouse TGF-β1 DuoSet enzyme-linked immunosorbent assay (R&D Systems) with modified manufacturer's instructions, whereby 100 µl supernatant was incubated with the capture antibody overnight on a shaker at 4 °C, not for 2 h at room temperature (RT). Optical density was measured in a plate reader (Bio-Rad) at 450 nm, with correction at 540 nm. Concentrations were obtained based on a regression equation (multimember regression, order 3) from the standard curve values (calculated in Microsoft Excel v16.16.20).

A cytometric bead array for Th1/Th2/Th17 cytokines was obtained from BD Biosciences and performed on 10 µl supernatant after 4-day coculture following the manufacturer's instructions, using a BD Fortessa2, and analysed following the manufacturer's template based on a standard curve for each cytokine.

PEG–peptide conjugate synthesis/characterization and hydrogel formation. Custom-designed peptides (supplied as either trifluoroacetic acid or acetate salts) used to create either $A_2 + B_4$ (Ac–CREW–ERC–NH_2) or $A_4 + B_4$ designs containing either a DEG (Ac–GRDSGK–GPQG↓IWGQ–ERC–NH_2), non-adhesive/non-degradable (NON-ADH/NON-DEG, Ac–KDW–ERC–NH_2) or adhesive sequence (RGD, presented in either a linear Ac–RGDSGK–GDQGIAGF–ERC–NH_2 or loop configuration (RGDSGD)K–GDQGIAGF–ERC–NH_2) were synthesized by Peptide Protein Research (all >98% purity). To create PEG–peptide

conjugates, peptide was dissolved in anhydrous dimethyl sulfoxide (Sigma) at 10 mg ml^{-1} and anhydrous triethylamine (Sigma) was added stoichiometrically to convert the peptide salts into their free forms in order to deprotonate the primary amine from the lysine side chain. Peptides were then conjugated to PEG-4NPC by a nucleophilic substitution reaction between the primary amine on the side chain of the lysine residue of each peptide and NPC esters, forming stable carbamate linkages. To accomplish this, a 16.67-mg-ml^{-1} solution of 10K (relative molecular mass 10,000) PEG-4NPC (JenKem Technology, USA) in dimethyl sulfoxide was reacted with peptide on an orbital shaker at either a 12:1 ratio of excess peptide to PEG-4NPC at RT for 30 min (NON-ADH/NON-DEG), a 10:1 ratio at 60 °C for 3 h (DEG), a 8:1 ratio at RT for 2 h (cyclic adhesive) or a 4:1 ratio at RT for 30 min (linear adhesive). Conjugates were then snap frozen on dry ice and lyophilized. To reduce disulfide bonds, conjugates were dissolved in carbonate–bicarbonate buffer at pH 9.0 and treated with dithiothreitol (0.1 g ml^{-1}) for 6 h at RT after nitrogen purging (molar ratio of 4.5:1 dithiothreitol:peptide). Conjugates were then purified four times in Milli-Q water using Merck Millipore ultrafiltration 1MWCO units (10-kDa cutoff), snap frozen and lyophilized again prior to storage at −20 °C.

Conjugation conversion was determined for NON-ADH/NON-DEG, DEG and cyclic adhesive conjugates by size exclusion chromatography using a Gilson high-performance liquid chromatography system. Calibration was performed using standards of known peptide concentration. The relative amount of unreacted peptide was assessed by estimating the concentration of free peptide in the crude reaction mixture. We observed that 77–87% of PEG arms were conjugated with peptide and that the conjugation efficiency was 81–91%.

Hydrogels with an A_4+B_4 design were formed by reacting PEG–peptide conjugates with PEG-4VS. The reaction was performed in a stoichiometric ratio of 1:1 in 30 mM HEPES buffer (pH 8.0, with 1× HBSS in a desired volume) through a Michael-type reaction between a cysteine thiol on the C terminus of the peptide and the vinyl sulfone group on PEG-4VS. To form 2.5% NON-ADH/NON-DEG hydrogels for swelling and rheological studies using an A_2+B_4 design, Ac–CREW–ERC–NH_2 was reacted with PEG-4VS in a stoichiometric ratio of 2:1 in 30-mM HEPES buffer (pH 8.0). Hydrogels were then allowed to form for 45–60 min prior to being placed in PBS/culture medium as indicated.

The conjugation efficiency of the thiol vinyl sulfone reaction was determined using proton NMR and Ellman's assay. For ^{1}H NMR experiments, PEG–peptide conjugate and PEG-4VS were dissolved separately in HEPES buffer and lyophilized. The resulting powders were dissolved separately in deuterium oxide to a final polymer/peptide concentration of 1.5 wt%, mixed at stoichiometric ratio and loaded into 0.3-mm-diameter NMR tubes. Acquisition of spectra was performed on a Bruker 700-MHz NMR spectrometer. The first measurement was made after 6 min and additional measurements collected for up to 1 h, when aromatic signals from the vinyl sulfone were no longer distinguishable. Hydrogel formation was observed inside the NMR tubes at the end of the experiment.

The relative quantities of free thiols during the reaction were quantified using the molar absorptivity of Ellman's reagent. Briefly, a 4-mg-ml^{-1} solution of Ellman's reagent was prepared in reaction buffer (0.1-M PBS, pH 8.0, containing 1-mM EDTA). Hydrogels were prepared and the crosslinking reaction halted after 5, 10, 15, 30 and 60 min using a 1:50 dilution of reaction buffer and Ellman's reagent solution. Samples were then incubated for 15 min and absorbance measured at 412 nm. Free thiols in a peptide (Ac–KDWERC–NH_2) solution alone were quantified using the same method. The concentration of free thiols was calculated based on the molar extinction coefficient of Ellman's reagent (14,150 M^{-1} cm^{-1}) and the following equation:

$$c = A/b\varepsilon$$

where A is the absorbance of the sample at 412 nm, b is 1 cm and ε is the molar extinction coefficient.

Molecular dynamics simulations. Coarse-grained classical molecular dynamics simulations were used to study the crosslinking of hydrogels formed with either A_4+B_4 or A_2+B_4 design. Three hydrogel systems were simulated in replicate: Ac–KDWERC–NH_2 and H–SREWERC–NH_2 are A_4+B_4 designs and Ac–CREWERC–NH_2 is an A_2+B_4 design. As in our experimental work, Ac–KDWERC–NH_2 and H–SREWERC–NH_2 are 'preconjugated' in the simulation to PEG-4NPC and the reaction with PEG-4VS is simulated. For Ac–CREWERC–NH_2, there was no preconjugation step and PEG-4VS was allowed to react with the free peptide. Ac–KDWERC–NH_2 is the NON-ADH/NON-DEG peptide used in experimental studies; however, as the net charge of Ac–KDWERC–NH_2 is −1, while that of Ac–CREWERC–NH_2 is 0, we also simulated the A_4+B_4 system with H–SREWERC–NH_2 (net charge of 0) to study our system independently of electrostatic bias in bond formation. Supplementary Fig. 17 summarizes the number of molecules and water beads used in each simulated system. As we have used the Martini forcefield to represent the peptide crosslinkers, ions and water molecules, each water bead represents four water molecules. The PEG molecules were modelled with a Martini-like forcefield, as described by Lee et al.[43,44].

The initial systems were built using PACKMOL (version 18.104)[45] to randomly place each component within a 40 nm × 40 nm × 40 nm simulation box. The LAMMPS simulation engine was used for all simulations[46]. The software package Moltemplate (version 2.7.3) was used[46] to convert the configurations generated by PACKMOL to ones readable by LAMMPS. The resulting systems have PEG concentrations of 2.5%. Once the initial systems were built, we first minimized energy using the steepest-descent algorithm with an energy tolerance of 1×10^{-4} and a force tolerance of 1×10^{-6}. The systems were then equilibrated by carrying out a series of simulations with the *NVT* (constant number of particles, volume and temperature) ensemble with the Langevin thermostat and a target temperature of 300 K. During these simulations, the systems were run for 1 ps with a 1 fs timestep, 3 ps with a 3 fs timestep, 10 ps with a 10 fs timestep and then 400 ps with a 20 fs timestep. The volume was then equilibrated by carrying out a series of simulations with the *NPT* (constant number of particles, pressure and temperature) ensemble employing the Langevin thermostat and the Parrinello–Rahman barostat. In these simulations, the timestep was again increased (1 ps with a 1 fs timestep, 3 ps with a 3 fs timestep, 10 ps with a 10 fs timestep and 2 ns with a 20 fs timestep). The densities of the systems were then equilibrated using the *NPT* ensemble with a Nosé-Hoover thermostat and barostat for a simulation lasting 2 ns with a 20 fs timestep. Finally, we equilibrated the temperature of the simulated systems to 450 K using an *NVT* simulation with the Nosé-Hoover thermostat, which lasted 40 ns with a 20 fs timestep.

Production simulations were carried out in the *NVT* ensemble at 450 K (to increase diffusion and allow for investigation of hydrogel crosslinking in a reasonable amount of simulation time) with a timestep of 20 fs. During simulations, we employed crosslinking methods that have been previously shown in simulations to lead to the formation of hydrogels[47]. In short, we identify beads that can react with one another and then check at regular time intervals (t_{react}) if any two reaction partner beads are within a given distance (r_{react}) of one another. If so, then a new bond is formed with a given probability (p_{react}). Here, we used a bead containing the sulfur atom within the cysteine residue on each peptide as a reactive bead in the simulations. Its reaction partner was the terminal bead on each arm of PEG-4VS. This reaction model is consistent with the chemistry that forms the hydrogels. The reactions were modelled using $t_{react}=20$ ps, $r_{react}=5.0$ Å and $p_{react}=0.5$. Once a bond was formed between any cysteine bead and a terminal bead on a PEG-4VS, neither of these beads could form any other new bonds during the simulation. Production simulations were run for at least 5.5 μs for one replica of each system, and the other replica was run for ~4 μs.

Measurements of hydrogel swelling. 30-μl hydrogels were formed in Sigmacote-treated 6-mm-diameter glass cylindrical moulds and submersed in PBS. Hydrogel weight was monitored, and the wet weight measured once swelling equilibrium had been achieved (after 48 h). Hydrogels were then lyophilized to determine dry weight and Q_m calculated using

$$Q_m = \text{wet weight}/\text{dry weight}$$

Rheological measurements of hydrogel gelation. Hydrogel gelation was assessed on a strain-controlled ARES from TA Instruments using a 25-mm cone of 0.02-rad by carrying out small-amplitude oscillatory time-sweep measurements at a strain of 5% and a constant angular frequency of 1 rad s^{-1}. All measurements were carried out at 37 °C, and low-viscosity paraffin oil was applied around the edge of the sample to prevent evaporation. To perform measurements, 80-μl hydrogels were placed on the lower plate of the instrument, and storage modulus G' and loss modulus G'' were recorded as a function of time in Orchestrator (version 7.2.0.2) software. Subsequently an amplitude sweep was carried out, recording G' and G'' as a function of shear amplitude in the range of 1–100% shear strain at a frequency of 1 rad s^{-1}, to determine the linear viscoelastic region. Finally, a frequency sweep was recorded, measuring G' and G'' as a function of shear frequency in a range of 100–0.1 rad s^{-1} at 5% shear strain to assess the hydrogels' temporal behaviour.

Quantification of MMP-mediated hydrogel degradation. Degradability was assessed on 30-μl hydrogels formed with either 0, 45, 75 or 100% of PEG–peptide conjugates containing a DEG sequence (all other crosslinks formed with NON-ADH/NON-DEG peptides) that had been allowed to swell in PBS for 24 h. To degrade hydrogels, PBS was replaced with a solution of TCNB buffer (50-mM Tris, pH 7.5, with 100-mM NaCl, 10-mM $CaCl_2$) containing 89.5-nM human MMP9 (Sigma SAE0078) and incubated at 37 °C. Degradation was determined by measuring the absorbance of tryptophan found on the cleaved peptide section in the supernatant at 280 nm. Degradation was determined by calculating the ratio of the cleaved peptide in solution to that in the initial hydrogel.

Mechanical testing by AFM-based indentation. 30-μl hydrogels were formed in Sigmacote-treated 6-mm-diameter glass cylindrical moulds in 35-mm petri dishes and stored in PBS at 4 °C prior to testing. Force–distance measurements were carried out on a JPK NanoWizard 4 (JPK Instruments) directly on hydrogels immersed in PBS at RT. To perform indentation measurements, spherical glass beads (diameter 10 μm; Whitehouse Scientific) were mounted on tipless triangular silicon nitride cantilevers (spring constant (K) ≈ 0.12 N m^{-1}; Bruker AFM Probes) using ultraviolet-crosslinked Loctite superglue. The deflection sensitivity of the AFM photodiode was then calibrated by collecting a single force–distance curve on a glass slide. Cantilevers were calibrated using the thermal method[48] in air. Measurements were made at six different locations across each hydrogel's surface

(100-μm × 100-μm areas, 100 force curves per location on three independent hydrogels per condition). Indentations were carried out with a relative setpoint force of 3 nN and a loading rate of 4 μm s^{-1}. Data were collected using JPK proprietary SPM software (version 6.1, JPK Instruments). The Oliver–Pharr model for a spherical tip was used to determine *E*. Outliers were removed using a ROUT test (Q = 1%). As for other hydrated biological samples, we assumed that volume was conserved and assigned a Poisson's ratio of 0.5.

Human aILC1 hydrogel cocultures. HIO were harvested and thoroughly rinsed with ice-cold PBS, then resuspended in pH-8.0 buffered phenol-free and protein-free HBSS (pH8-HBSS, Gibco), spun down, resuspended and left on ice until encapsulation. PEG–peptide conjugates were dissolved in ice-cold pH8-HBSS, vortexed and centrifuged, and combined based on the gel composition (for example, IM-DEG: 20% cyclic adhesive, 45% DEG, 35% NON-DEG). An equal molar mass of PEG-4VS was weighed in a protein-low-binding Eppendorf tube, dissolved in pH8-HBSS, centrifuged and added to the PEG–conjugate mix, and the sample was vortexed and centrifuged again. HIO were then rapidly mixed into the PEG–peptide conjugate/PEG-4VS mix using protein-low-binding 200-μl tips, and pipetted into a prewarmed, Sigmacote-treated glass ring in a 24-well Nunclon plate. HIO-laden gels were incubated at 37 °C, and after 30 min the glass ring was removed using autoclaved forceps. Basal medium supplemented with 50-mM β-mercaptoethanol, 20-ng-ml^{-1} IL-2, 20-ng-ml^{-1} IL-7 and 1-ng-ml^{-1} IL-15 (R&D), containing FACS-isolated human ILC1 from inflamed biopsies, was added to the cultures.

Stiffness mapping of IM-DEG hydrogel-HIO cultures by AFM. Organoids were encapsulated in IM-DEG hydrogels formed in Sigmacote-treated 10-mm-diameter glass cylindrical moulds and submersed in culture medium. Force–distance curves were collected on a JPK NanoWizard-CellHesion (JPK Instruments) mounted on an inverted light microscope. Tipless triangular silicon nitride cantilevers ($K \approx 0.12$ N m^{-1}; Bruker AFM Probes) were calibrated using the thermal method[48] in air and then functionalized with 50-μm glass beads (Cospheric) as above. Prior to measurements, the deflection sensitivity of the AFM photodiode was calibrated by collecting a single force–distance curve on a glass slide in liquid.

Prior to measurements, cultures containing organoids were placed in CO_2-independent medium (Sigma). Maps were then collected across the surfaces of hydrogels in regions where an organoid could be clearly identified on the inverted light microscope. Map sizes varied depending on the organoid size but indentations were done in either 8 × 8 or 16 × 16 grids, with the largest map being 300 × 300 μm^2 and the smallest 150 × 150 μm^2. For each map, indentations were carried out at a relative setpoint of 2.5 nN and a loading rate of 4 μm s^{-1}. The manufacturer's proprietary JPK SPM software (version 6.1, JPK Instruments) was used to determine *E* using the Hertz model for a spherical tip. As for other hydrated biological samples, we assumed that volume was conserved and assigned a Poisson's ratio of 0.5.

Multiple-particle-tracking microrheology. 0.75-μm-diameter fluorescent beads (Fluoresbrite YG carboxylate kit I 21636-1, Polysciences) were suspended at a concentration of 0.04% (w/w) in the polymer solution within 5–10-μl HIO-laden hydrogels with or without aILC1. Samples were prepared and imaged in ibidi slide chambers (μ-Slide Angiogenesis, 81501) using a set-up and analysis pipeline modified from that previously described by Schultz et al.[28]. Approximately 7–10 HIO were embedded in each hydrogel.

Time-lapses of moving beads were acquired using an Olympus TIRF system using an excitation of 488 nm. Time-lapses of 800 frames were collected at a rate of 16.9 ms per frame and exposure time of 1.015 ms. HIO images were also captured in bright field. Three to eight experimental measurements were made for each sample. TrackMate (Fiji, version 4.0.1) was used to segment beads and create trajectories across the 800 frames. Mean squared displacements of individual beads were then calculated from the TrackMate output using custom R-script (Supplementary Dataset 2).

Immunocytochemistry. Cocultures were fixed for 10 min using 4% paraformaldehyde and either stained as whole organoids in FCS-coated Eppendorf tubes or cryoprotected (overnight 30% glucose for organoids in Matrigel, overnight optimal cutting temperature compound replacement for hydrogels) and embedded in optimal cutting temperature compound for cryosectioning on a Penguin cryostat. Images were acquired on an Leica SP8 inverted confocal microscope. Cells were blocked with 2% FCS and 0.05% Triton X in PBS for 1 h at RT, stained at 4 °C overnight, and in secondaries (Thermo Fisher) for 1 h at RT, followed by extensive rinse steps. Heat antigen retrieval was performed in pH-8.0 basic conditions (10 min, 95-°C waterbath) for CD44v6 staining to reveal the v6 epitope, and optimize signal strength. All secondary antibodies were Alexa Fluor conjugate dyes (488, 555 or 647) raised in donkey (Thermo Fisher).

Image processing and quantification was performed using Fiji (version 1.0, ImageJ). Image quantification was performed on maximum-intensity projections with (1) the same number of *z* stacks and (2) the same brightness and contrast settings in each fluorophore channel, having been taken with the same laser power and gain values. The background intensity of the channel was subtracted from the average intensity, which was then normalized to DAPI (nuclear) intensity. Nuclear phosphorylated p38 (P-p38) was quantified as follows: the DAPI channel was processed to 'binary' and erosion (E) and dilation (D) operations were performed to homogenize the nucleus area (E, D, D, E). An overlay with the outlines of the nuclei was created and saved in the ROI manager, which was then superimposed on either P-p38 channel. The mean intensity of each fluorophore within the defined nuclei areas was measured, giving an approximate measure of intensity values/nucleus. A list of antibodies and dilutions used is provided in Supplementary Table 2.

Viability tests. A single-cell viability test distinguishing between epithelial cells (EpCAM$^+$, CD90$^-$) and fibroblasts (EpCAM$^-$, CD90$^+$) was performed using a fixable LIVE/DEAD near-infrared viability kit (Thermo Fisher). Encapsulated HIO were rinsed with PBS, then treated with 0.025% trypsin–EDTA (Gibco) for 10-20 min at 37 °C to dissociate both the hydrogel and the HIO. HIO were then rinsed with PBS, stained with LIVE/DEAD near-infrared for 15 min at 4 °C in the dark, then stained for 20 min with EpCAM–FITC and CD90–PE/Dazzle for 20 min at 4 °C in the dark in PBS with 2% FCS. Dissociated HIO were analysed on a BD Fortessa2. Whole HIO viability within the gel was assessed by rinsing the gel twice with PBS, then staining HIO with 5-mg-ml^{-1} fluorescein diacetate (FDA; Sigma-Aldrich, C-7521) and 2-mg-ml^{-1} propidium iodide (Sigma-Aldrich, P4170) in PBS for 2 min while gently shaking, followed by two rinse steps with PBS. HIO–hydrogel conditions were treated and imaged one at a time, and images acquired within 1–10 min of FDA/PI treatment to ensure that comparable FDA levels were acquired and no excess cytotoxicity was induced through the treatment process. Images were captured at ×20 on a Leica SP8 confocal microscope, and only HIO at the bottom of the gel within the complete *z*-stack range were acquired. Flow cytometry was quantified with FlowJo (version 10.5.3); images were quantified using Fiji (version 1.0).

Production of RNA-seq dataset. The cells were harvested as described above for sorting by flow cytometry (BD ARIA3 Fusion using BD FACS Diva 8.0.1 software) into RLT (QIAGEN) lysis buffer. RNA was harvested using an RNeasy MicroRNA isolation kit (QIAGEN), and RIN values were assessed using an RNA 6000 Pico Kit (Agilent). The library was prepared using SMART-Seq2 and sequenced using an Illumina HiSeq 4000 at the Wellcome Trust Oxford Genomics Core, where basic alignment (GRCm38.ERCC (2011)) and quality control were also performed.

RNA-seq data analysis. *Exploratory data analysis and filtering.* The data count matrix was filtered for genes with a mean of less than 3 to remove very low-count genes, and genes where most of the counts were zero were also removed.

Model description. A varying intercepts hierarchical modelling framework was used to model the expression for each gene. This analysis was implemented in R[49] and Stan[50].

Pathway analysis. Gene set enrichment analysis was carried out using the R package GAGE, and predicted upstream regulators, canonical pathways, and diseases and functions were determined using IPA (version 01–13, QIAGEN) of $p_{adj} < 0.05$ genes, excluding chemicals.

hMSC attachment on 2D hydrogel surfaces. Human bone-marrow-derived stromal cells (hMSC) were obtained from the Imperial College Healthcare Tissue Bank (ICHTB, Human Tissue Authority licence 12275). ICHTB is supported by the National Institute for Health Research (NIHR) Biomedical Research Centre based at Imperial College Healthcare NHS Trust and Imperial College London. ICHTB is approved by the UK National Research Ethics Service to release human material for research (12/WA/0196) as previously described[51]. The samples for this project were issued from subcollection R160052. Fifty-microlitre 5% hydrogels formed with 5-K PEG-4VS were formed in six-well plates and 24-mm Sigmacote-treated coverslips placed on top. After hydrogel formation, 5,000 hMSC cm^{-2} were seeded and allowed to adhere for 2 h prior to the addition of basal culture medium. After 24 h, hMSC were fixed in 4% paraformaldehyde, permeabilized in 0.2% (v/v) Triton X-100 and stained with phalloidin–tetramethylrhodamine isothiocyanate (Sigma) and DAPI. Cells were imaged on an Olympus inverted fluorescent microscope equipped with a Jenoptik camera.

Animals. CD45.1 mice (B6.SJL-*Ptprc^{a}Pepc^b*/BoyCrl, female, 6–8 weeks) were purchased from Charles River and *Rorc(γt)-Gfp^{TG}* reporter mice[52] (female, 6–10 weeks) were a gift from G. Eberl (Institut Pasteur, Paris, France).

Both animal lines were maintained at Charles River (Margate) and in the New Hunt's House King's College London animal facilities by Biological Services Unit staff. Animals were maintained with enrichment in specific pathogen-free conditions with a 12-h light/12-h dark cycle, at ~19–22 °C and ~50% humidity in accordance with the UK Animals (Scientific Procedures) Act 1986 (UK Home Office Project License PPL:70/7869 to September 2018; P9720273E from September 2018).

Statistics. Statistical analyses were performed in GraphPad Prism version 8.1.2.

Reporting Summary. Further information on research design is available in the Nature Research Reporting Summary linked to this article.

Data availability

The differentially expressed genes identified in the RNA-seq dataset are available in Supplementary Dataset 1. The data have also been deposited with GEO at https://www.ncbi.nlm.nih.gov/sra/?term=PRJNA641809 and at https://github.com/uhkniazi/BRC_Organoids_Geraldine. All other data supporting the findings of this study are available within the article and its supplementary information files or from the corresponding authors upon reasonable request.

Code availability

All codes used to analyse the molecular dynamics simulations were tools that were built in house. All codes with accompanying documentation on how to use them are freely accessible at https://github.com/Lorenz-Lab-KCL and https://nms.kcl.ac.uk/lorenz.lab/wp/. R code for determining α from mean squared displacement data for microrheology is available in Supplementary Dataset 2 and is freely accessible at https://github.com/eileengentleman/Microrheology-code.

References

39. Sato, T. & Clevers, H. Primary mouse small intestinal epithelial cell cultures. *Methods Mol. Biol.* **945**, 319–328 (2013).
40. Gronke, K., Kofoed-Nielsen, M. & Diefenbach, A. in *Methods in Molecular Biology* Vol. 1559 (eds Clausen, B. & Laman, J.) 255–265 (Humana, 2017).
41. Di Marco Barros, R. et al. Epithelia use butyrophilin-like molecules to shape organ-specific γδ T cell compartments. *Cell* **167**, 203–218.e17 (2016).
42. Omer, O. S., Powell, N. & Lord, G. M. Characterizing innate lymphoid cell phenotype and function in human inflammatory bowel disease. In *Innate Lymphoid Cells. Methods in Molecular Biology* (ed. Amarnath, S.) Vol. 2121 (Humana, 2020).
43. de Jong, D. H. et al. Improved parameters for the Martini coarse-grained protein force field. *J. Chem. Theory Comput.* **9**, 687–697 (2013).
44. Lee, H., de Vries, A. H., Marrink, S. & Pastor, R. W. A coarse-grained model for polyethylene oxide and polyethylene glycol: conformation and hydrodynamics. *J. Phys. Chem. B* **113**, 13186–13194 (2009).
45. Martínez, L., Andrade, R., Birgin, E. G. & Martínez, J. M. PACKMOL: a package for building initial configurations for molecular dynamics simulations. *J. Comput. Chem.* **30**, 2157–2164 (2009).
46. Plimpton, S. Fast parallel algorithms for short-range molecular dynamics. *J. Comput. Phys.* **117**, 1–19 (1995).
47. Bode, F. et al. Hybrid gelation processes in enzymatically gelled gelatin: impact on nanostructure, macroscopic properties and cellular response. *Soft Matter* **9**, 6986–6999 (2013).
48. Hutter, J. L. & Bechhoefer, J. Calibration of atomic-force microscope tips. *Rev. Sci. Instrum.* **64**, 1868–1873 (1993).
49. Luo, W., Friedman, M. S., Shedden, K., Hankenson, K. D. & Woolf, P. J. GAGE: generally applicable gene set enrichment for pathway analysis. *BMC Bioinform.* **10**, 161 (2009).
50. Carpenter, B. et al. Stan: a probabilistic programming language. *J. Stat. Softw.* **76**, 1–32 (2017).
51. Ferreira, S. A. et al. Bi-directional cell-pericellular matrix interactions direct stem cell fate. *Nat. Commun.* **9**, 4049–12 (2018).
52. Lochner, M. et al. In vivo equilibrium of proinflammatory IL-17$^+$ and regulatory IL-10$^+$ Foxp3$^+$ RORγt$^+$ T cells. *J. Exp. Med.* **205**, 1381–1393 (2008).

Acknowledgements

G.M.J. acknowledges a PhD fellowship from the Wellcome Trust (203757/Z/16/A) and a BRC Bright Sparks Precision Medicine Early Career Research Award. E.G. acknowledges a Philip Leverhulme Prize from the Leverhulme Trust. J.F.N. acknowledges a Marie Skłodowska-Curie Fellowship, a King's Prize fellowship, an RCUK/UKRI Rutherford Fund fellowship (MR/R024812/1) and a Seed Award in Science from the Wellcome Trust (204394/Z/16/Z). J.F.N. and E.G. are grateful to the Gut Human Organoid Platform (Gut-HOP) at King's College London, which is supported financially by a King's Together Strategic Award. M.D.A.N. is supported by a PhD studentship funded by the BBSRC London Interdisciplinary Doctoral Programme. E.R. acknowledges a PhD fellowship from the Wellcome Trust (215027/Z/18/Z). S.T.L. gratefully acknowledges the UK Medical Research Council (MR/N013700/1) for funding through the MRC Doctoral Training Partnership in Biomedical Sciences at King's College London. G.M.L. is supported by grants awarded by the Wellcome Trust (091009) and the Medical Research Council (MR/M003493/1 and MR/K002996/1). N.J.W. acknowledges a Jane and Aatos Erkko Foundation Personal Scholarship. R.M.P.d.S. acknowledges a King's Prize fellowship supported by the Wellcome Trust (Institutional Strategic Support Fund), King's College London and the London Law Trust. Via C.D.L.'s membership in the UK's HEC Materials Chemistry Consortium, which is funded by EPSRC (EP/L000202, EP/R029431), this work used the ARCHER UK National Supercomputing Service (http://www.archer.ac.uk) and the UK Materials and Molecular Modelling Hub (MMM Hub) for computational resources, which is partially funded by EPSRC (EP/P020194/1), to carry out the molecular dynamics simulations. We also thank the BRC flow cytometry core team, and acknowledge financial support from the Department of Health via the NIHR comprehensive Biomedical Research Centre award to Guy's and St. Thomas' NHS Foundation Trust in partnership with King's College London and King's College Hospital NHS Foundation Trust. The views expressed are those of the authors and not necessarily those of the NHS, the NIHR or the Department of Health. We thank C. Dondi, D. Foyt and O. Birch for technical assistance. We are grateful to J. Spencer and K. Schultz for helpful conversations about CD44 and microrheology, R. Beavil and A. Beavil for technical support with size exclusion chromatography–high-performance liquid chromatography, H. Sinclair from the Microscopy Innovation Centre for assistance acquiring microrheology data, R. Thorogate and the London Centre for Nanotechnology for assistance with AFM, R. A. Atkinson and the NMR Facility of the Centre for Biomolecular Spectroscopy at King's College London, which was established with awards from the Wellcome Trust, British Heart Foundation and King's College London, for assistance with NMR, and S. Engledow at the Oxford Wellcome Genomics Centre for processing the RNA-seq samples. Finally, we thank L. Roberts, E. Slatery and R. Sancho for critically reading this manuscript and providing helpful feedback.

Author contributions

G.M.J., M.D.A.N., T.T.L.Y., L.B., J.F.N. and E.G. developed experimental protocols, conducted experiments and analysed data. G.M.J. designed, conducted and analysed all murine and human experiments. T.T.L.Y., J.H., O.P.O., N.J.W., N.D.E., E.G. and R.M.P.d.S. designed and optimized the hydrogel synthesis. R.M.P.d.S. designed peptide sequences. M.D.A.N., D.H., S.T.L., T.T.L.Y., G.M.J., C.A.D. and D.M. characterized the hydrogel. S.T.L. and C.D.L. performed the molecular dynamics simulations. G.M.J. and J.F.N. designed the RNA-seq experiment, and U.N. and M.W.H.C. provided bioinformatic analysis. G.M.J., P.R.A., E.R. and T.Z. performed tissue isolations. G.M.J., E.G., M.D.A.N. and E.H. designed and conducted microrheology and AFM experiments. G.M.L., O.S.O. and D.D. contributed reagents, biopsies and hiPSC lines. G.M.J., E.G. and J.F.N. conceived the ideas, initiated the project, interpreted the data and prepared the manuscript. E.G. and J.F.N. supervised the project. All authors revised the manuscript.

Competing interests

The authors declare no competing interests.

Additional information

Supplementary information is available for this paper at https://doi.org/10.1038/s41563-020-0783-8.

Correspondence and requests for materials should be addressed to J.F.N. or E.G.

Reprints and permissions information is available at www.nature.com/reprints.

nature research

Corresponding author(s): Eileen Gentleman, Joana F. Neves

Last updated by author(s): 2020/06/18

Reporting Summary

Nature Research wishes to improve the reproducibility of the work that we publish. This form provides structure for consistency and transparency in reporting. For further information on Nature Research policies, see Authors & Referees and the Editorial Policy Checklist.

Statistics

For all statistical analyses, confirm that the following items are present in the figure legend, table legend, main text, or Methods section.

n/a	Confirmed	
☐	☒	The exact sample size (*n*) for each experimental group/condition, given as a discrete number and unit of measurement
☐	☒	A statement on whether measurements were taken from distinct samples or whether the same sample was measured repeatedly
☐	☒	The statistical test(s) used AND whether they are one- or two-sided *Only common tests should be described solely by name; describe more complex techniques in the Methods section.*
☐	☒	A description of all covariates tested
☐	☒	A description of any assumptions or corrections, such as tests of normality and adjustment for multiple comparisons
☐	☒	A full description of the statistical parameters including central tendency (e.g. means) or other basic estimates (e.g. regression coefficient) AND variation (e.g. standard deviation) or associated estimates of uncertainty (e.g. confidence intervals)
☐	☒	For null hypothesis testing, the test statistic (e.g. *F*, *t*, *r*) with confidence intervals, effect sizes, degrees of freedom and *P* value noted *Give P values as exact values whenever suitable.*
☐	☒	For Bayesian analysis, information on the choice of priors and Markov chain Monte Carlo settings
☐	☒	For hierarchical and complex designs, identification of the appropriate level for tests and full reporting of outcomes
☒	☐	Estimates of effect sizes (e.g. Cohen's *d*, Pearson's *r*), indicating how they were calculated

Our web collection on statistics for biologists contains articles on many of the points above.

Software and code

Policy information about availability of computer code

Data collection	Data collection software is indicated in the methods, and includes TrackMate (v. 4.0.1) for microrheology, PACKMOL (v. 18.104) and Moltemplate (v. 2.7.3) for molecular dynamics, JPK SPM software (v. 6.1) for AFM, LAS X for confocal microscopy, BD FACS Diva8.0.1 for FACS, and Orchestrator (v. 7.0) for rheological data collection.
Data analysis	Detailed methods, software, and scripts used for RNA-sequencing dataset analysis are available at https://www.evernote.com/l/ASDhP0E8zgZA256MQRNRG62FUHzfi4fhO5s/ as well as at https://github.com/uhkniazi/BRC_Organoids_Geraldine All of the code that was used to analyse the molecular dynamics simulations were tools that were built in-house. All these codes and documentation as to how to use them are available at https://github.com/Lorenz-Lab-KCL and https://nms.kcl.ac.uk/lorenz.lab/wp/ for the public to access and use freely. Microrheology data were analysed using custom R-code available in Supplementary dataset 2 and at https://github.com/eileengentleman/Microrheology-code. AFM data analysis was performed using JPK SPM software (v. 6.1). Orchestrator software (v. 7.0) was used for rheological data analysis. Excel (Microsoft, v. 16.16.20) was used for RT-qPCR, swelling, crypt budding, ELISA, ellmans, and CBA analysis. FlowJo (v. 10.5.3) was used for flow cytometry analysis. GSEA was performed using the R-package GAGE. IPA analysis was carried out using IPA (v. 01-13, Qiagen). Fiji (v. 1.0) was used for image analysis. Graphpad (version 8.1.2) was used for statistics.

For manuscripts utilizing custom algorithms or software that are central to the research but not yet described in published literature, software must be made available to editors/reviewers. We strongly encourage code deposition in a community repository (e.g. GitHub). See the Nature Research guidelines for submitting code & software for further information.

Data

Policy information about availability of data

All manuscripts must include a data availability statement. This statement should provide the following information, where applicable:

- Accession codes, unique identifiers, or web links for publicly available datasets
- A list of figures that have associated raw data
- A description of any restrictions on data availability

The differentially expressed genes identified in the RNAsequencing dataset (Figure 1) are available in the Supplementary dataset1, and the unrestricted, full dataset is deposited at https://www.ncbi.nlm.nih.gov/sra/?term=PRJNA641809

Field-specific reporting

Please select the one below that is the best fit for your research. If you are not sure, read the appropriate sections before making your selection.

☒ Life sciences ☐ Behavioural & social sciences ☐ Ecological, evolutionary & environmental sciences

For a reference copy of the document with all sections, see nature.com/documents/nr-reporting-summary-flat.pdf

Life sciences study design

All studies must disclose on these points even when the disclosure is negative.

Sample size	No statistical method was used to pre-determine sample size. All sample sizes, statistical tests and p-values are indicated in the figure legends, and comprehensively described in the supplementary "Statistical reporting" file appended to the manuscript. In the murine studies, each experiment was performed by isolating ILC1 from 3-5 litter-controlled animals (females) that were heterozygous for RORγt-GFP+, which each represented one biological replicate (N). Where inhibitors were used, ILC1 from the same mouse were split into two wells, allowing for direct comparison of the treatment to a biologically matched control. For immunofluorescence analysis, 3-10 organoids were analysed per biological replicate. For human studies, each biological replicate was defined as co-cultures established from ILC1 isolated from a different patient biopsy, and the experiments were independently repeated at least three times, and performed on three separate rounds of intestinal organoid differentiations. For atomic force microscopy measurements, 50-70 force curves were collected per force map area, and each individual experiment was from organoids from the same round of differentiation encapsulated into the same batch of hydrogels to limit variability.
Data exclusions	Force curves acquired by atomic force microscopy that did not meet the QC requirements described in Supplementary Fig. 22 were excluded from analyses in Figs. 5b,c. No other data were excluded from other analyses.
Replication	All replication experiments were successful. Murine organoids were derived from 4 different CD45.1 mice over the course of the paper, a minimum of 6 indepenent human organoid differentiations were used for the human studies, and all ILC1 were derived from biologically distinct organisms/patients.
Randomization	Samples were prepared, treated, processed and analyzed in a random order.
Blinding	With the exception of crypt bud quantification, which was blinded, the investigators were not blinded during this experiment, as the same investigators who set up the experiments carried out the analysis, which was incompatible with complete blinding.

Reporting for specific materials, systems and methods

We require information from authors about some types of materials, experimental systems and methods used in many studies. Here, indicate whether each material, system or method listed is relevant to your study. If you are not sure if a list item applies to your research, read the appropriate section before selecting a response.

Materials & experimental systems

n/a	Involved in the study
☐	☒ Antibodies
☐	☒ Eukaryotic cell lines
☒	☐ Palaeontology
☐	☒ Animals and other organisms
☐	☒ Human research participants
☒	☐ Clinical data

Methods

n/a	Involved in the study
☒	☐ ChIP-seq
☐	☒ Flow cytometry
☒	☐ MRI-based neuroimaging

Antibodies

Antibodies used

All antibodies used in this study were purchased commercially, the details of which are reported in the Methods section. We give the supplier, product code, host species, species reactivity, and dilution used.

CD45-eFluor450 (HI30; Invitrogen), Lineage cocktail 3-FITC (CD3, CD14, CD19, CD20; BD Biosciences) CD4-FITC (OKT4; BioLegend), TCRα/β-FITC (IP26; Biolegend),
TCRγ/δ-FITC (B1; Biolegend), CD56-Alexa700 (B159; BD Pharmingen), CD7-PE-CF594 (M-T701; BD Horizon),
CD127-PE-Cy7 (eBioRDR5; Invitrogen), c-kit-BV605 (104D2; BioLegend), CRTH2-PE (MACS Milltenyi Biotec),CD161-APC (HP-3G10; BioLegend). CD45-eFluor450(HI30) InvitrogenEpCAM-FITC (9C4; BioLegend) CD90-PE/Dazzle (Thy1; BioLegend)CD44-PE (IM7, BioLegend) EpCAM–APC Cy7 (G8.8, BioLegend), CD45-BV510 (30-F11, bioLegend), NK1.1 BV605 (PK136, BioLegend), CD3-Fluor450 (RB6-8C5), CD5-Fluor450 (53-7.3) CD19-Fluor450 (eBio1D3), Ly6G-Fluor450 (RB6-8C5), CD45-BV510 (30-F11, bioLegend), CD127-APC (A7R34), KLRG1-PerCP/eFluor710 (2F1), NKp46-PE/Cyanine7 (29A1.4), NK1.1-PE (PK136), Fibronectin abcam Ab2413, CD45 (HI30) BioLegend 30400, 1FoxA2 Abcam Ab108422, CDX2 Abcam Ab76541, Lyzozyme Invitrogen PA5-16668, E-Cadherin (DECMA-1) eBioscience 51-3249-82, β-catenin BD Biosciences 610153, CD44 (IM7) eBioscience 14-0551-82, EpCAM abcam Ab71916, GATA4 Santa Cruz Sc-25310, SOX17 R&D Af1924, Vimentin Millipore Ab5733, TGFβR1 Santa Cruz Sc-339, ZO-1 ThermoFisher 61-7300, Phos- p38 (Thr180/Tyr182) Cell Signalling 4511, CD44var6 (VFF-18) ThermoFisher BMS125, CD44v6 (9A4) BioRad MCA1967, SMA R&D MAB142, β-catenin R&D AF1329

Validation

Antibodies were purchased that had been previously published (and validated by the manufacturer):

Fibronectin abcam Ab2413 "(1) Lionarons DA et al. RAC1P29S Induces a Mesenchymal Phenotypic Switch via Serum Response Factor to Promote Melanoma Development and Therapy Resistance. Cancer Cell 36:68-83.e9 (2019).
"(2) Gao L et al. TNAP inhibition attenuates cardiac fibrosis induced by myocardial infarction through deactivating TGF-ß1/Smads and activating P53 signaling pathways. Cell Death Dis 11:44 (2020).
(3) Zhang Z et al. Stepwise Adipogenesis of Decellularized Cellular Extracellular Matrix Regulates Adipose Tissue-Derived Stem Cell Migration and Differentiation. Stem Cells Int 2019:1845926 (2019).
CD45 BioLegend 304001 Each lot of this antibody is quality control tested by immunofluorescent staining with flow cytometric analysis. For flow cytometric staining, the suggested use of this reagent is ≤ 0.5 µg per 106 cells in 100 µl volume or 100 µl of whole blood. (1)Kishihara K, et al. 1993. Cell 74:143
(2)Morozov A, et al. 2010. Clin Cancer Res. 16:5630. PubMed (3)Rees LE, et al. 2003. Clin. Exp. Immunol. 134:497. (IF)

FoxA2 Abcam Ab108422 (1) Shafa M et al. Long-Term Stability and Differentiation Potential of Cryopreserved cGMP-Compliant Human Induced Pluripotent Stem Cells. Int J Mol Sci 21:N/A (2019).
(2) Momozane T et al. Efficient Differentiation of Mouse Induced Pluripotent Stem Cells into Alveolar Epithelium Type II with a BRD4 Inhibitor. Stem Cells Int 2019:1271682 (2019).
(3) Wang J et al. Hepatocyte Nuclear Factor 3ß Plays a Suppressive Role in Colorectal Cancer Progression. Front Oncol 9:1096 (2019).
CDX2 Abcam Ab76541 (1) Stock AA et al. Conformal Coating of Stem Cell-Derived Islets for ß Cell Replacement in Type 1 Diabetes. Stem Cell Reports 14:91-104 (2020)
(2) Gerdtsson AS et al. Single cell correlation analysis of liquid and solid biopsies in metastatic colorectal cancer. Oncotarget 10:7016-7030 (2019)
(3) Frith TJR & Tsakiridis A Efficient Generation of Trunk Neural Crest and Sympathetic Neurons from Human Pluripotent Stem Cells Via a Neuromesodermal Axial Progenitor Intermediate. Curr Protoc Stem Cell Biol N/A:e81 (2019)
Lyzozye Invitrogen PA5-16668 (1) Igarashi M, Miura M, Williams E, et al. NAD+supplementation rejuvenates aged gut adult stem cells. Aging Cell. 2019;18(3):e12935. doi:10.1111/acel.12935
Immunofluorescence analysis of Lysozyme was performed using 70% confluent log phase Hep G2 cells. The cells were fixed with 4% paraformaldehyde for 10 minutes, permeabilized with 0.1% Triton™ X-100 for 15 minutes, and blocked with 2% BSA for 1 hour at room temperature. The cells were labeled with Lysozyme Polyclonal Antibody (Product # PA5-16668) at 1:100 dilution in 0.1% BSA, incubated at 4 degree Celsius overnight and then labeled with Goat anti-Rabbit IgG (H+L) Superclonal™ Recombinant Secondary Antibody, Alexa Fluor® 488 conjugate (Product # A27034) at a dilution of 1:2000 for 45 minutes at room temperature (Panel a: green). (2) Akcora D, Huynh D, Lightowler S, et al. The CSF-1 receptor fashions the intestinal stem cell niche. Stem Cell Res. 2013;10(2):203-212. doi:10.1016/j.scr.2012.12.001
(3) Gomi H, Osawa H, Uno R, et al. Canine Salivary Glands: Analysis of Rab and SNARE Protein Expression and SNARE Complex Formation With Diverse Tissue Properties. J Histochem Cytochem. 2017;65(11):637-653. doi:10.1369/0022155417732527
E-Cadherin (DECMA-1) eBioscience 51-3249-82 (1) Ören B, Urosevic J, Mertens C, et al. Tumour stroma-derived lipocalin-2 promotes breast cancer metastasis. J Pathol. 2016;239(3):274-285. doi:10.1002/path.4724
2) Palen K, Weber J, Dwinell MB, Johnson BD, Ramchandran R, Gershan JA. E-cadherin re-expression shows in vivo evidence for mesenchymal to epithelial transition in clonal metastatic breast tumor cells. Oncotarget. 2016;7(28):43363-43375. doi:10.18632/oncotarget.9715
(3) Zheng X, Carstens JL, Kim J, et al. Epithelial-to-mesenchymal transition is dispensable for metastasis but induces chemoresistance in pancreatic cancer. Nature. 2015;527(7579):525-530. doi:10.1038/nature16064
B-catenin BD Biosciences 610153 (1) Eger A, Stockinger A, Schaffhauser B, Beug H, Foisner R. Epithelial mesenchymal transition by c-Fos estrogen receptor activation involves nuclear translocation of beta-catenin and upregulation of beta-catenin/lymphoid enhancer binding factor-1 transcriptional activity. J Cell Biol. 2000; 148(1):173-187.
(2) Fallone F, Britton S, Nieto L, Salles B, Muller C. ATR controls cellular adaptation to hypoxia through positive regulation of hypoxia-inducible factor 1 (HIF-1) expression. Oncogene. 2013; 32(37):4387-4396.
(3) Persad S, Troussard AA, McPhee TR, Mulholland DJ, Dedhar S. Tumor suppressor PTEN inhibits nuclear accumulation of beta-catenin and T cell/lymphoid enhancer factor 1-mediated transcriptional activation. J Cell Biol. 2001; 153(6):1161-1173
CD44 (IM7) eBioscience 17-0441-82
Staining of C57BL/6 splenocytes with staining buffer (autofluorescence) (open histogram) or 0.03 µg of Anti-Human/Mouse

CD44 APC (filled histogram). Total viable cells were used for analysis. (1) Liu Z, Ge Y, Wang H, et al. Modifying the cancer-immune set point using vaccinia virus expressing re-designed interleukin-2. Nat Commun. 2018;9(1):4682. Published 2018 Nov 8. doi:10.1038/s41467-018-06954-z

(2) Huang W, Bei L, Eklund EA. Inhibition of Fas associated phosphatase 1 (Fap1) facilitates apoptosis of colon cancer stem cells and enhances the effects of oxaliplatin. Oncotarget. 2018;9(40):25891-25902. Published 2018 May 25. doi:10.18632/oncotarget.25401

(3) Cao Y, Lin SH, Wang Y, Chin YE, Kang L, Mi J. Glutamic Pyruvate Transaminase GPT2 Promotes Tumorigenesis of Breast Cancer Cells by Activating Sonic Hedgehog Signaling. Theranostics. 2017;7(12):3021-3033. Published 2017 Jul 22. doi:10.7150/thno.18992

Epcam abcam Ab71916 https://www.abcam.com/ps/products/71/ab71916/Images/ab71916-316641-anti-epcam-antibody-immunofluorescence.jpg (1) Joshi PA et al. PDGFRa+ stromal adipocyte progenitors transition into epithelial cells during lobulo-alveologenesis in the murine mammary gland. Nat Commun 10:1760 (2019)

ab71916 staining EpCam in HT29 cells. The cells were fixed with 100% methanol (5min), permeabilized with 0.1% Triton X-100 for 5 minutes and then blocked with 1% BSA/10% normal goat serum/0.3M glycine in 0.1%PBS-Tween for 1h. The cells were then incubated overnight at +4°C with ab71916 at 1µg/ml and ab7291, Mouse monoclonal [DM1A] to alpha Tubulin - Loading Control, at 1/1000 dilution. Cells were then incubated with ab150120, Goat polyclonal Secondary Antibody to Mouse at 1/1000 dilution (shown in pseudocolour red) and ab150081, Goat polyclonal Secondary Antibody to Rabbit IgG at 1/1000 dilution (shown in green). Nuclear DNA was labelled with DAPI (shown in blue). (2) Xu W et al. Establishment of pancreatic cancer patient-derived xenograft models and comparison of the differences among the generations. Am J Transl Res 11:3128-3139 (2019).

(3) Fukui E et al. Adipose Tissue-Derived Stem Cells Have the Ability to Differentiate into Alveolar Epithelial Cells and Ameliorate Lung Injury Caused by Elastase-Induced Emphysema in Mice. Stem Cells Int 2019:5179172 (2019).

GATA4 Santa Cruz Sc-25310

GATA-4 (G-4) Alexa Fluor® 546: sc-25310 AF546. Direct immunofluorescence staining of formalin-fixed SW480 cells showing nuclear localization. Blocked with UltraCruz® Blocking Reagent: sc-516214.

SOX17 R&D Af1924 (1) Wang X, Liao T, Wan C, et al. Efficient generation of human primordial germ cell-like cells from pluripotent stem cells in a methylcellulose-based 3D system at large scale. PeerJ. 2019;6:e6143. Published 2019 Jan 9. doi:10.7717/peerj.6143

SOX17 in B16 Mouse Cell Line. SOX17 was detected in immersion fixed B16 mouse melanoma cell line using 10 µg/mL Goat Anti-Human SOX17 Antigen Affinity-purified Polyclonal Antibody (Catalog # AF1924) for 3 hours at room temperature. Cells were stained with the NorthernLights™ 557-conjugated Anti-Goat IgG Secondary Antibody (red; Catalog # NL001) and counter-stained with DAPI (blue). View our protocol for Fluorescent ICC Staining of Cells on Coverslips. (2) Diekmann U, Wolling H, Dettmer R, Niwolik I, Naujok O, Buettner FFR. Chemically defined and xenogeneic-free differentiation of human pluripotent stem cells into definitive endoderm in 3D culture. Sci Rep. 2019;9(1):996. Published 2019 Jan 30. doi:10.1038/s41598-018-37650-z

(3) Broda TR, McCracken KW, Wells JM. Generation of human antral and fundic gastric organoids from pluripotent stem cells. Nat Protoc. 2019;14(1):28-50. doi:10.1038/s41596-018-0080-z

Vimentin Millipore Ab5733 "(1) A systems view of epithelial-mesenchymal transition signaling states.
Thomson, S; Petti, F; Sujka-Kwok, I; Mercado, P; Bean, J; Monaghan, M; Seymour, SL; Argast, GM; Epstein, DM; Haley, JD
Clinical & experimental metastasis 28 137-55 2011"

"(2) Semaphorin7A regulates neuroglial plasticity in the adult hypothalamic median eminence.
Parkash, J; Messina, A; Langlet, F; Cimino, I; Loyens, A; Mazur, D; Gallet, S; Balland, E; Malone, SA; Pralong, F; Cagnoni, G; Schellino, R; De Marchis, S; Mazzone, M; Pasterkamp, RJ; Tamagnone, L; Prevot, V; Giacobini, P
Nature communications 6 6385 2015"

"(3) Inhibition of TGFβ signaling increases direct conversion of fibroblasts to induced cardiomyocytes.
Ifkovits, JL; Addis, RC; Epstein, JA; Gearhart, JD
PloS one 9 e89678 2014"

TGFBR1 Santa Cruz sc-518018

ZO-1 Thermofisher 61-7300 (1) Balmer D, Bapst-Wicht L, Pyakurel A, et al. Bis-Retinoid A2E Induces an Increase of Basic Fibroblast Growth Factor via Inhibition of Extracellular Signal-Regulated Kinases 1/2 Pathway in Retinal Pigment Epithelium Cells and Facilitates Phagocytosis. Front Aging Neurosci. 2017;9:43. Published 2017 Mar 1. doi:10.3389/fnagi.2017.00043

Immunofluorescent analysis of ZO-1 (green) in Caco-2 cells. The cells were fixed with 4% paraformaldehyde for 15 minutes and blocked with 3% Blocker BSA (Product # 37525) in PBS for 15 minutes at room temperature. Cells were stained with or without ZO-1 rabbit polyclonal antibody (Product # 61-7300), at a concentration of 5 µg/mL for 1 hour at room temperature, and then incubated with a Goat anti-Rabbit IgG (H+L) Superclonal Secondary Antibody, Alexa Fluor® 488 conjugate (Product # A27034) at a dilution of 1:1000 for 1 hour at room temperature (both panels, green). Nuclei (both panels, blue) were stained with Hoechst 33342 dye (Product # 62249). Images were taken on a Thermo Scientific ToxInsight at 20X magnification (2) Shukla PK, Meena AS, Rao V, Rao RG, Balazs L, Rao R. Human Defensin-5 Blocks Ethanol and Colitis-Induced Dysbiosis, Tight Junction Disruption and Inflammation in Mouse Intestine. Sci Rep. 2018;8(1):16241. Published 2018 Nov 2. doi:10.1038/s41598-018-34263-4

(3) Li S, Zhou J, Zhang L, et al. Ectodysplasin A regulates epithelial barrier function through sonic hedgehog signalling pathway. J Cell Mol Med. 2018;22(1):230-240. doi:10.1111/jcmm.13311

Phos-p38 Cell Signalling 4511 (1) Yang Z, Chen Y, Wei X, Wu D, Min Z, Quan Y. Upregulated NTF4 in colorectal cancer promotes tumor development via regulating autophagy. Int J Oncol. 2020;56(6):1442-1454. doi:10.3892/ijo.2020.5027

Immunohistochemical analysis of paraffin-embedded human colon carcinoma using Phospho-p38 MAPK (Thr180/Tyr182) (D3F9) XP® Rabbit mAb. (2) Mercer HL, Snyder LM, Doherty CM, Fox BA, Bzik DJ, Denkers EY. Toxoplasma gondii dense granule protein GRA24 drives MyD88-independent p38 MAPK activation, IL-12 production and induction of protective immunity. PLoS Pathog. 2020;16(5):e1008572. Published 2020 May 15.

(3) Xiao H, Jiang Y, He W, et al. Identification and functional activity of matrix-remodeling associated 5 (MXRA5) in benign hyperplastic prostate. Aging (Albany NY). 2020;12(9):8605-8621. doi:10.18632/aging.103175

Phalloidin-TexRed "Thermofisher
" T7471 "(1) A new family of Cdc42 effector proteins, CEPs, function in fibroblast and epithelial cell shape changes.
Hirsch DS, Pirone DM, Burbelo PD
J Biol Chem (2001) 276:875-883"

Fixed, permeabilized bovine pulmonary artery endothelial cells were labeled with Texas Red®-X phalloidin (Cat. no. T7471), which stains F-actin, and counterstained with DAPI (Cat. no. D1306, D3571, D21490). The panels show the unprocessed image (upper panel), after deconvolution (middle panel) and after deconvolution and three-dimensional reconstruction (lower panel). The image was deconvolved using Huygens software (Scientific Volume Imaging, http://www.svi.nl/). 3-D reconstruction was

performed using Imaris software (Bitplane AG, http://www.bitplane.com/). (2) Sekerková G, Zheng L, Loomis PA, et al. Espins are multifunctional actin cytoskeletal regulatory proteins in the microvilli of chemosensory and mechanosensory cells. J Neurosci. 2004;24(23):5445-5456. doi:10.1523/JNEUROSCI.1279-04.2004

(3) Spessotto P, Rossi FM, Degan M, et al. Hyaluronan-CD44 interaction hampers migration of osteoclast-like cells by down-regulating MMP-9. J Cell Biol. 2002;158(6):1133-1144. doi:10.1083/jcb.200202120

DAPI Thermofisher D1306 (1) Kessels MM, Engqvist-Goldstein AE, Drubin DG. Association of mouse actin-binding protein 1 (mAbp1/SH3P7), an Src kinase target, with dynamic regions of the cortical actin cytoskeleton in response to Rac1 activation. Mol Biol Cell. 2000;11(1):393-412. doi:10.1091/mbc.11.1.393

(2) Micchelli CA, Perrimon N. Evidence that stem cells reside in the adult Drosophila midgut epithelium. Nature. 2006;439(7075):475-479. doi:10.1038/nature04371

(3) Davaadelger B, Choi MR, Singhal H, Clare SE, Khan SA, Kim JJ. BRCA1 mutation influences progesterone response in human benign mammary organoids. Breast Cancer Res. 2019;21(1):124. Published 2019 Nov 26. doi:10.1186/s13058-019-1214-0

CD44var6 (Vff-18) Thermofisher BMS125 (1) Vermeulen JF, van Brussel AS, Adams A, et al. Near-infrared fluorescence molecular imaging of ductal carcinoma in situ with CD44v6-specific antibodies in mice: a preclinical study. Mol Imaging Biol. 2013;15(3):290-298. doi:10.1007/s11307-012-0605-8

(2) Casucci M, Nicolis di Robilant B, Falcone L, et al. CD44v6-targeted T cells mediate potent antitumor effects against acute myeloid leukemia and multiple myeloma. Blood. 2013;122(20):3461-3472. doi:10.1182/blood-2013-04-493361

Only 2 cited for staining

CD44v6 (9A4) Biorad MCA1967 "(1) Boon, E.M. et al. (2006) Activation of Wnt signaling in the intestinal mucosa of Apc +/min mice does not cause overexpression of the receptor tyrosine kinase Met.
Cancer Sci. 97: 710-5."

"(2) Termeer, C. et al. (2003) Targeting dendritic cells with CD44 monoclonal antibodies selectively inhibits the proliferation of naive CD4+ T-helper cells by induction of FAS-independent T-cell apoptosis.
Immunology. 109: 32-40."

"(3) Shibata, W. et al. (2017) Helicobacter-induced gastric inflammation alters the properties of gastric tissue stem/progenitor cells.
BMC Gastroenterol. 17 (1): 145."

SMA R&D MAB142 (1) Savarese TM, Campbell CL, McQuain C, et al. Coexpression of oncostatin M and its receptors and evidence for STAT3 activation in human ovarian carcinomas. Cytokine. 2002;17(6):324-334. doi:10.1006/cyto.2002.1022

"(2) Chopin V, Slomianny C, Hondermarck H, Le Bourhis X. Synergistic induction of apoptosis in breast cancer cells by cotreatment with butyrate and TNF-alpha, TRAIL, or anti-Fas agonist antibody involves enhancement of death receptors' signaling and requires P21(waf1). Exp Cell Res. 2004;298(2):560-573. doi:10.1016/j.yexcr.2004.04.038
"

(3) Harris LK, Keogh RJ, Wareing M, et al. Invasive trophoblasts stimulate vascular smooth muscle cell apoptosis by a fas ligand-dependent mechanism. Am J Pathol. 2006;169(5):1863-1874. doi:10.2353/ajpath.2006.060265

B_catenin R&D AF1329 (1) Udagawa T, Harita Y, Miura K, et al. Amnionless-mediated glycosylation is crucial for cell surface targeting of cubilin in renal and intestinal cells. Sci Rep. 2018;8(1):2351. Published 2018 Feb 5. doi:10.1038/s41598-018-20731-4

(2) Reuter S, Martin H, Beckert H, et al. The Wnt/β-catenin pathway attenuates experimental allergic airway disease. J Immunol. 2014;193(2):485-495. doi:10.4049/jimmunol.1400013

(3) Sáenz-Morales D, Escribese MM, Stamatakis K, et al. Requirements for proximal tubule epithelial cell detachment in response to ischemia: role of oxidative stress. Exp Cell Res. 2006;312(19):3711-3727. doi:10.1016/j.yexcr.2006.05.024

CD45-eFluor450 (HI30; Invitrogen) 48-0451-82 https://pubmed.ncbi.nlm.nih.gov/30455690/
https://pubmed.ncbi.nlm.nih.gov/30181538/
https://pubmed.ncbi.nlm.nih.gov/17661344/

Lineage cocktail 3-FITC (CD3, CD14, CD19, CD20; BD Biosciences) 643510 https://www.cdc.gov/mmwr/preview/mmwrhtml/00000039.htm
https://pubmed.ncbi.nlm.nih.gov/16462794/
https://www.jimmunol.org/content/179/7/4654

CD4-FITC (OKT4; BioLegend) 317407 https://pubmed.ncbi.nlm.nih.gov/22851709/
https://pubmed.ncbi.nlm.nih.gov/26302932/
https://pubmed.ncbi.nlm.nih.gov/30221739/

TCRα/β-FITC (IP26; Biolegend) 306705 https://pubmed.ncbi.nlm.nih.gov/26878113/
https://pubmed.ncbi.nlm.nih.gov/29491406/
https://pubmed.ncbi.nlm.nih.gov/31751473/

TCRγ/δ-FITC (B1; Biolegend) 331207 https://pubmed.ncbi.nlm.nih.gov/26297765/
https://pubmed.ncbi.nlm.nih.gov/29491406/
https://pubmed.ncbi.nlm.nih.gov/31751473/

CD56-Alexa700 (B159; BD Pharmingen) 557919 https://www.ncbi.nlm.nih.gov/nlmcatalog/9514353

CD7-PE-CF594 (M-T701; BD Horizon) 562541 https://trove.nla.gov.au/work/17305164?q&versionId=20292739
https://www.jimmunol.org/content/152/2/517.abstract
Barclay NA, Brown MH, Birkeland ML, et al, ed. The Leukocyte Antigen FactsBook. San Diego, CA: Academic Press; 1997 (there was also this reference but I couldn't find a link for it :/)

CD127-PE-Cγ7 (eBioRDR5; Invitrogen) 25-1278-42 https://pubmed.ncbi.nlm.nih.gov/29271540/
https://pubmed.ncbi.nlm.nih.gov/29907650/
https://pubmed.ncbi.nlm.nih.gov/28290464/

c-kit-BV605 (104D2; BioLegend) 313217 https://pubmed.ncbi.nlm.nih.gov/17379743/

https://pubmed.ncbi.nlm.nih.gov/29045900/
https://pubmed.ncbi.nlm.nih.gov/31840071/

CRTH2-PE (MACS Milltenyi Biotec) 130-113-600 https://pubmed.ncbi.nlm.nih.gov/9973380/
https://europepmc.org/article/med/11069080
https://pubmed.ncbi.nlm.nih.gov/12447360/

CD161-APC (HP-3G10; BioLegend) 339911 https://pubmed.ncbi.nlm.nih.gov/9730888/
https://pubmed.ncbi.nlm.nih.gov/29343684/
https://pubmed.ncbi.nlm.nih.gov/27898686/

EpCAM-FITC (9C4; BioLegend) 324203 https://pubmed.ncbi.nlm.nih.gov/12063020/
https://pubmed.ncbi.nlm.nih.gov/31548591/
https://pubmed.ncbi.nlm.nih.gov/32111836/

CD90-PE/Dazzle (Thy1; BioLegend) 328133 https://pubmed.ncbi.nlm.nih.gov/7683034/
https://onlinelibrary.wiley.com/doi/full/10.1002/cyto.b.20530
https://www.ncbi.nlm.nih.gov/pmc/articles/PMC3582577/

CD44-PE (IM7, BioLegend) 103023 https://link.springer.com/article/10.1007/BF00364338
https://pubmed.ncbi.nlm.nih.gov/22961052/
https://pubmed.ncbi.nlm.nih.gov/24842756/

CD45-BV510 (30-F11, bioLegend) 103137 https://pubmed.ncbi.nlm.nih.gov/16709810/
https://pubmed.ncbi.nlm.nih.gov/31101805/
https://pubmed.ncbi.nlm.nih.gov/31073183/

NK1.1 BV605 (PK136, BioLegend) 108739 https://pubmed.ncbi.nlm.nih.gov/18523245/
https://pubmed.ncbi.nlm.nih.gov/30709740/
https://pubmed.ncbi.nlm.nih.gov/31801072/

CD19-Fluor450 (eBio1D3) 48-0193-82 https://pubmed.ncbi.nlm.nih.gov/21490158/
https://pubmed.ncbi.nlm.nih.gov/30258845/
https://pubmed.ncbi.nlm.nih.gov/29354128/

Ly6G-Fluor450 (RB6-8C5) 48-5931-82 https://pubmed.ncbi.nlm.nih.gov/17877537/
https://pubmed.ncbi.nlm.nih.gov/29619244/
https://pubmed.ncbi.nlm.nih.gov/29765026/

CD127-APC (A7R34) 135011 https://pubmed.ncbi.nlm.nih.gov/21209281/
https://pubmed.ncbi.nlm.nih.gov/27752043/
https://pubmed.ncbi.nlm.nih.gov/30970254/

KLRG1-PerCP/eFluor710 (2F1) 46-5893-82 https://pubmed.ncbi.nlm.nih.gov/24037376/
https://pubmed.ncbi.nlm.nih.gov/28197366/
https://pubmed.ncbi.nlm.nih.gov/30356668/

NKp46-PE/Cyanine7 (29A1.4) 25-3351-82 https://pubmed.ncbi.nlm.nih.gov/21874025/
https://pubmed.ncbi.nlm.nih.gov/28815219/
https://pubmed.ncbi.nlm.nih.gov/29150606/

NK1.1-PE (PK136) 12-5941-82 https://pubmed.ncbi.nlm.nih.gov/12847141/
https://pubmed.ncbi.nlm.nih.gov/28713327/
https://pubmed.ncbi.nlm.nih.gov/30254309/

Eukaryotic cell lines

Policy information about cell lines

Cell line source(s)

The feeder-free KUTE-4 human induced pluripotent stem cell line was derived from skin tissue via CytoTune 2 in 2015, as part of the HipSci consortium phenotyping project by senior author Davide Danovi (Kilpinen, H., Goncalves, A., Leha, A. et al. Common genetic variation drives molecular heterogeneity in human iPSCs. Nature 546, 370–375 (2017). https://doi.org/10.1038/nature22403). The cell line is banked at ECACC, the disease status of the anonymous donor was normal, the and all phenotyping information and pluripotency scores for this line can be found at http://www.hipsci.org/lines/#/lines/HPSI0714i-kute_4. The authors acknowledges Wellcome Trust Sanger Institute as the source of Kute-4 human induced pluripotent cell line.

R-Spondin 1 conditioned medium was produced using Cultrex HA-R-Spondin1-Fc 293T Cells, the provider of the cell line and

the Materials Transfer Agreement was the Board of Trustees of the Leland Stanford Junior University (Calvin Kuo, MD, PhD, Stanford University)

Noggin-conditioned media was obtained from the HEK-293T-mNoggin-Fc cell line, which was obtained through a Material Transfer Agreement with the Hubrecht Institute, Uppsalalaan 8, 3584 CT Utrecht, The Netherlands, and is based on the publication by Farin, Van Es & Clevers Gastroenterology (2012).

Authentication

TThe KUTE-4 cell line (low passage number, p24), was extensively phenotyped (karyotype, SNPs, methylome), without any attempt to identify the original donor. The results of the authentication can be found at http://www.hipsci.org/lines/#/lines/HPSI0714i-kute_4.

We performed functional authentication of the R-Spondin- and Noggin-producing cell lines through the QC of each batch of conditioned media, where we cultured organoids with conditioned media, media with corresponding recombinant growth factors, or without growth factors. Growth factor withdrawal results in visible organoid differentiation followed by organoid cell death within three days. The conditioned media was able to recapitulate the phenotypes of the corresponding growth factors (R-Spondin1 – crypt maintenance, Noggin-inhibition of differentiation).

Mycoplasma contamination

Cell lines were periodically tested for mycosplasma by the Centre for Stem Cells and Regenerative Medicine research assistants, and tested mycoplasma negative.

Commonly misidentified lines
(See ICLAC register)

No commonly misidentified lines were used for experiments in this study.

Animals and other organisms

Policy information about studies involving animals; ARRIVE guidelines recommended for reporting animal research

Laboratory animals

CD45.1 mice (B6.SJL-PtprcaPepcb/BoyCrl, female, 6-8 weeks) were purchased from Charles River and Rorc(γt)-GfpTG reporter mice (female, 6-10 weeks) were a kind gift from Gérard Eberl.

Both animal lines were maintained at Charles River (Margate) and in the New Hunt's House KCL animal facilities by BSU staff. Animals were maintained with enrichment in SPF conditions with a 12 light/12 dark cycle, at ~19-22°C and ~50% humidity.

Wild animals

No wild animals were used in this study.

Field-collected samples

No field-collected samples were used in this study.

Ethics oversight

All animals were housed under specific pathogen-free conditions at accredited Charles River and King's College London animal units in accordance with the UK Animals (Scientific Procedures) Act 1986 (UK Home Office Project License (PPL:70/7869 to September 2018; P9720273E from September 2018).

Note that full information on the approval of the study protocol must also be provided in the manuscript.

Human research participants

Policy information about studies involving human research participants

Population characteristics

Biopsies were obtained with informed consent from adult donors during routine endoscopy procedures for Inflammatory Bowel Disease (IBD). Active or inactive inflammation status of IBD patients was diagnosed by the gastroenterology consultant. Patients were male-63:37-female, Crohn's disease-27:73-Ulcerative colitis, and patients were age 24-84 (median age 34, mean age 42), and all biopsies were taken from the colon. Only the inflammation status was considered, and the disease classification, sex, and age were not treated as confounding factors, as plotting the data based on these covariates did not reveal any significant differences in CD44v6 expression or in hydrogel matrix properties.

Human MSC samples used in this research project the Imperial College Healthcare Tissue Bank (ICHTB, HTA license 12275). ICHTB is supported by the National Institute for Health Research (NIHR) Biomedical Research Centre based at Imperial College Healthcare NHS Trust and Imperial College London. Clinical-grade, bone marrow-derived hMSC were generated from bone marrow (BM) aspirates collected from the iliac crest of healthy paediatric donors with informed consent. These cells were used to confirm adhesion properties of the cyclic adhesive peptide, and there were no relevant patient covariates to be assessed.

Recruitment

Participants were not recruited within this study.

Ethics oversight

Biopsies acquisition for lymphocyte isolation received ethical approval from the London Dulwich Research Ethics Committee (REC reference 15/LO/1998). Informed written consent was obtained in all cases.

Human MSC samples were obtained from the Imperial College Healthcare Tissue Bank (ICHTB, HTA license 12275). ICHTB is supported by the National Institute for Health Research (NIHR) Biomedical Research Centre based at Imperial College Healthcare NHS Trust and Imperial College London. ICHTB is approved by the UK National Research Ethics Service to release human material

for research (12/WA/0196), and the samples for this project were issued from sub-collection R16052. Informed written consent was obtained in all cases.

Note that full information on the approval of the study protocol must also be provided in the manuscript.

Flow Cytometry

Plots

Confirm that:

☒ The axis labels state the marker and fluorochrome used (e.g. CD4-FITC).

☒ The axis scales are clearly visible. Include numbers along axes only for bottom left plot of group (a 'group' is an analysis of identical markers).

☒ All plots are contour plots with outliers or pseudocolor plots.

☒ A numerical value for number of cells or percentage (with statistics) is provided.

Methodology

Sample preparation	Sample preparation is described in detail in the methods section. Cells were sorted in PBS buffer with 2% FCS using a 70micron nozzle (mouse samples) or 85micron nozzle (human samples).
Instrument	Cells were FACS purified on a BD Aria II or Aria III, and analysed on a BD Fortessa (cytometric bead array of supernatant).
Software	Flow cytometry data was analysed using FlowJo 10.4.1.
Cell population abundance	One mouse small intestine yielded approximately 1000-4000 type 1 innate lymphoid cells, and after co-culture approximately 10.000 IEC and 500-4000 ILC1 (depending on number of ILC1 seeded into co-culture) were purified from co-cultures. Approximately 15-18 biopsies yielded approximately 10million lymphocytes, of which 50-500 were CD161+ ILC1.
Gating strategy	Positive and negative populations were determined using appropriate FMOs when population separations were not visible by eye. ILC1 : LIVE, lineage (CD3,CD5,CD19,Ly6G)-, CD127+, RORγt-GFP-, KLRG1-, NKp46+, NK1.1+ IEC: LIVE, CD45-, EpCAM+ ILC1 post-co-culture: LIVE, CD45+ EpCAM- hILC1: Live, lineage- (CD3, CD4, CD14, CD19, TCRαβ, TCRγδ), CD7+, CD56-, CD127+, cKIT-, CRTh2-, CD161+ hIEC post-co-culture: LIVE, EpCAM+, CD45- hFibroblasts post-co-culture: LIVE, EpCAM+, CD45-, CD90+ hILC1: LIVE, EpCAM-, CD45+

☒ Tick this box to confirm that a figure exemplifying the gating strategy is provided in the Supplementary Information.